Spatiotemporal tracking of intracellular nanoparticles using complementary imaging systems reveals acute ferroptosis triggered by burst reduction of ferric ions

Chan-Gi Pack [a,b,1], Min Kyo Jung [c,1], Kyunghwan Kim [d,1], Woojung Yoo [e], Minjong Kim [f], Minju Cho [a,g], Myoung-Hee Kang [e], Sanghwa Lee [a,g], Jisu Im [e], In Ki Kim [a,b], Sang-Wook Lee [b,h], Jun Ki Kim [a,g,*], Jinmyoung Joo [e,i,j,k,**]

a Department of Biomedical Engineering, Brain Korea 21 Project, University of Ulsan College of Medicine, Seoul 05505, South Korea
b Convergence Medicine Research Center, Asan Institute for Life Sciences, Asan Medical Center, Seoul 05505, South Korea
c Department of Structure and Function of Neural Network, Korea Brain Research Institute, Daegu 41068, South Korea
d Department of Chemistry, Ulsan National Institute of Science and Technology (UNIST), Ulsan 44919, South Korea
e Department of Biomedical Engineering, Ulsan National Institute of Science and Technology (UNIST), Ulsan 44919, South Korea
f Department of Biological Science, Ulsan National Institute of Science and Technology (UNIST), Ulsan 44919, South Korea
g Biomedical Engineering Research Center, Asan Institute for Life Sciences, Asan Medical Center, Seoul 05505, South Korea
h Department of Radiation Oncology, University of Ulsan College of Medicine, Seoul 05505, South Korea
i Center for Genomic Integrity, Institute for Basic Science, Ulsan 44919, South Korea
j Graduate School of Health Science and Technology, Ulsan National Institute of Science and Technology (UNIST), Ulsan 44919, South Korea
k Materials Research Science and Engineering Center, University of California, San Diego, La Jolla, CA 92093, United States

ARTICLE INFO

ABSTRACT

Uptake and intracellular trafficking of nanoparticles are tightly regulated by their interactions with cellular organelles and physiological microenvironment. Although the dynamic physicochemical reactions at the interface of nanoparticles and cells ultimately determine the intracellular distribution and fate, microscopic tracing and quantitative analysis of the nanoparticles have been hampered by the limited resolution associated with individual nanoparticle trafficking. Herein, we report spatiotemporal investigations on autophagic clearance of biodegradable iron oxide-silica core-shell nanoparticles in terms of intracellular trafficking and ionic dissolution at a single cell level using multimodal imaging systems. By combining transmission electron microscopy and super-resolution confocal laser scanning microscopy with fluorescence correlation spectroscopy, the complementary imaging analysis exclusively shows the intracellular uptake, endosomal fusion and biodegradative clearance, leading to identify the step-by-step endocytic transport pathway and autophagic degradation pathways. Tracing the intracellular trafficking of nanoparticles reveals that they are spontaneously transported from endosomes to lysosomes, and transiently stimulate autophagy while maintaining cell viability. While protecting iron oxide core, the silica shell is gradually degraded during endocytosis and autophagic clearance, resulting in ionic dissolution of iron oxide in acidic environment. Moreover, burst reduction of ferric ions by adding ascorbic acid readily triggers acute ferroptosis owing to rapid supplement of ferrous ions and Fenton reaction in cancer cells. The complementary imaging strategy provides insights into the design of biocompatible nanomedicines for cellular delivery and the degradative mechanisms beyond the intracellular fate.

Introduction

Nanoparticles have attracted tremendous attention in biological science and biomedical technology as a promising toolbox because of the controllable physicochemical properties and useful functions to be adopted for studying the living organisms [1–3]. In particular, potential

applications of the nanoparticles for drug delivery systems, bioimaging, and theranostics have dramatically increased over the past decade. There has also been considerable interest on the interactions between nanoparticles and living systems in order to develop highly efficient nanomedicine with safe clinical implementation, as well as revealing environmental toxicology [3–6]. However, most of the studies has focused on the macroscopic analysis of nanoparticles such as therapeutic efficacy, cumulative cellular uptake and adverse cytotoxicity [7–13], while little attention has been paid to the spatiotemporal tracking of individual nanoparticles with respect to their mobility, intracellular interactions with organelles, and degradation process in the cell [14–16]. Although the intracellular trafficking of nanoparticles is critical characteristics to fully understand the interfacial phenomena and ultimate fate, tracing the dynamic interactions with cellular constituents at a single nanoparticles level has not yet been comprehensively investigated due to the lack of systematic analysis methods.

Cellular uptake of nanoparticles typically begins with their adherence to the outer cell membrane and the interactions with a variety of distinct molecular environments including lipids, protein complexes, and other components of the plasma membrane [17–19]. The endocytic pathway allows the nanoparticles to be internalized by forming a endosome, which traps the peripheral nanoparticles into the vesicles. The endocytic nanoparticles are transported into the cell, and further trafficked to different subcellular locations, typically ending in lysosomal degradation or exocytosis [20–23]. However, many questions remain regarding the fate of nanoparticles during the course of endocytosis [24]. For instance, little is currently known regarding: (i) the existence and rate of spontaneous nanoparticle escape from the endocytic pathway to cytosol, and (ii) whether escaped nanoparticles are freely mobile or able to target specific subcellular compartments. In addition, there is currently an inadequate understanding of: (iii) the degradation kinetics of lysosome-trapped nanoparticles and (iv) their cumulative behavior in the cell unless degraded. Such processes can be quantitatively addressed at a single nanoparticle level in the cell using complementary imaging analysis to provide an in-depth understanding of the interactions between nanoparticles and subcellular compartments. This information can be further used to advance the design of therapeutic nanoparticles.

Nanoparticles are recognized as foreign substances to the cell, thus activate the formation of autophagosomes, which then fuse to lysosomes to form autolysosomes to degrade these exotic nanoparticles [25–31]. Cellular autophagy is a regulated mechanism leading to the decomposition of unnecessary or dysfunctional intracellular components, resulting in ordered degradation. However, autophagy and lysosomal dysfunction induced by the nanoparticles has occasionally been observed to cause severe cellular toxicity, resulting in cell death and morbidity [32–34]. Therefore, autophagic clearance of the nanoparticles is considered a key factor in the development of biocompatible and biodegradable drug delivery carriers or imaging probes. Moreover, the nanoparticle-driven autophagic pathway and therapeutic strategies based on autophagy modulation should be understood in depth for a broad range of biomedical applications because autophagy has been implicated in various cellular processes and diseases, such as cancer and neurodegenerative diseases [35–39].

Here, we report the intracellular mobility of nanoparticles with spatiotemporal tracking and quantitative analysis using the complementary imaging system. Time-lapse super-resolution confocal laser scanning microscopy (CLSM), fluorescence correlation spectroscopy (FCS), and transmission electron microscopy (TEM) are demonstrated for systematic investigation on a spatiotemporal dynamics and intracellular distribution of biodegradable nanoparticles along with their interactions to cellular organelles. Fluorescent silica nanoparticles were used as a model probe due to the ease of surface modification, low cytotoxicity, and biodegradability [40–42]. Particularly, the biodegradative nature of the silica nanoparticles are of interest to be investigated as a promising drug carrier. To clearly visualize the location

of the silica nanoparticles in TEM, iron oxide nanoparticles were incorporated to form core-shell structure for clarifying imaging contrast and accuracy against the ultrastructure of cellular organelles, such as endosomes, autophagosomes, and lysosomes, without affecting their intracellular mobility. In addition, gradual degradation of silica shell represents not only spontaneous drug release but also exposure of iron oxide core in acidic microenvironment, followed by ionic dissolution. Burst reduction of ferrous ions by adding ascorbic acid readily triggers acute ferroptosis via Fenton reaction-induced lipid peroxidation. Although the intracellular trafficking of various nanoparticles has been reported in macroscopic point of view [43–45], we present the dynamic behavior of the biodegradable nanoparticles to address spatiotemporal states of individual nanoparticles in a cell. Finally, we examine the effect of nanoparticles on cellular autophagy, followed by investigating both biopersistence and biodegradation of the nanoparticles in the cell, in terms of modulated cancer cell death. To the best of our knowledge, this study is the first to spatiotemporally visualize nanoparticle-induced autophagosome formation and nanoparticle clearance using high-resolution correlative imaging systems. The present study not only provides an in-depth understanding of the dynamic nature of cellular responses upon nanoparticle uptake but also provides insight into the mechanisms needed for the rational design of nanoparticles for a variety of biomedical applications, including drug delivery and programmed cell death.

Results

Complementary imaging system for tracing intracellular nanoparticles

To investigate intracellular transport of nanoparticles in spatiotemporal manner, we configured the complementary imaging system using CLSM, FCS, and TEM (Fig. 1). Upon exposure to the cells, uptake and intracellular trafficking of nanoparticles can be firstly observed under CLSM analysis showing cytosolic distribution as a function of incubation time, followed by FCS analysis to obtain quantitative mobility of individual nanoparticles. With its high spatial resolution, the CLSM provides precise visualization of nanoparticle movement and real-time observation within complex intracellular environments, enabling to investigate interactions with cellular components. In addition, longitudinal studies to examine intracellular trafficking of nanoparticles permit long-term tracing for investigating the intricate interplay between nanoparticles and cellular structures. Quantitative analysis using FCS further presents high temporal resolution for monitoring fast-moving nanoparticles and dynamic intracellular processes based on diffusion and residence time of individual nanoparticles even at very low concentration level. Cells are then fixed and mounted on a copper grid to display the organelles and microstructures containing the intracellular nanoparticles. Therefore, the complementary correlative microscopic imaging analysis is considerably beneficial to obtain multiscale information on nanoparticle trafficking in a single cell level.

Intracellular trafficking and hydrodynamic characteristics of endocytic nanoparticles

We prepared $Fe_3O_4@SiO_2$ core@shell nanoparticles, which provide high contrast imaging capability for accurate analysis of the intracellular distribution of nanoparticles and their interactions with cellular compartments. The nanoparticles consisted of non-toxic Fe_3O_4 core and SiO_2 shell incorporated with rhodamine B isothiocyanate (RITC) which is not only used for fluorescent labeling but also considered as a model drug payloads (Fig. 2A). Thus, complementary imaging capability should be largely attributed to the tailored properties of the nanoparticles exhibiting both extensive electron density at the magnetic core (Fe_3O_4) for TEM and bright fluorescence emission at the shell (RITC-embedded SiO_2) for CLSM and FCS. The nanoparticles show a well-defined core@shell structure with narrow size distribution (Fig. 2B and C),
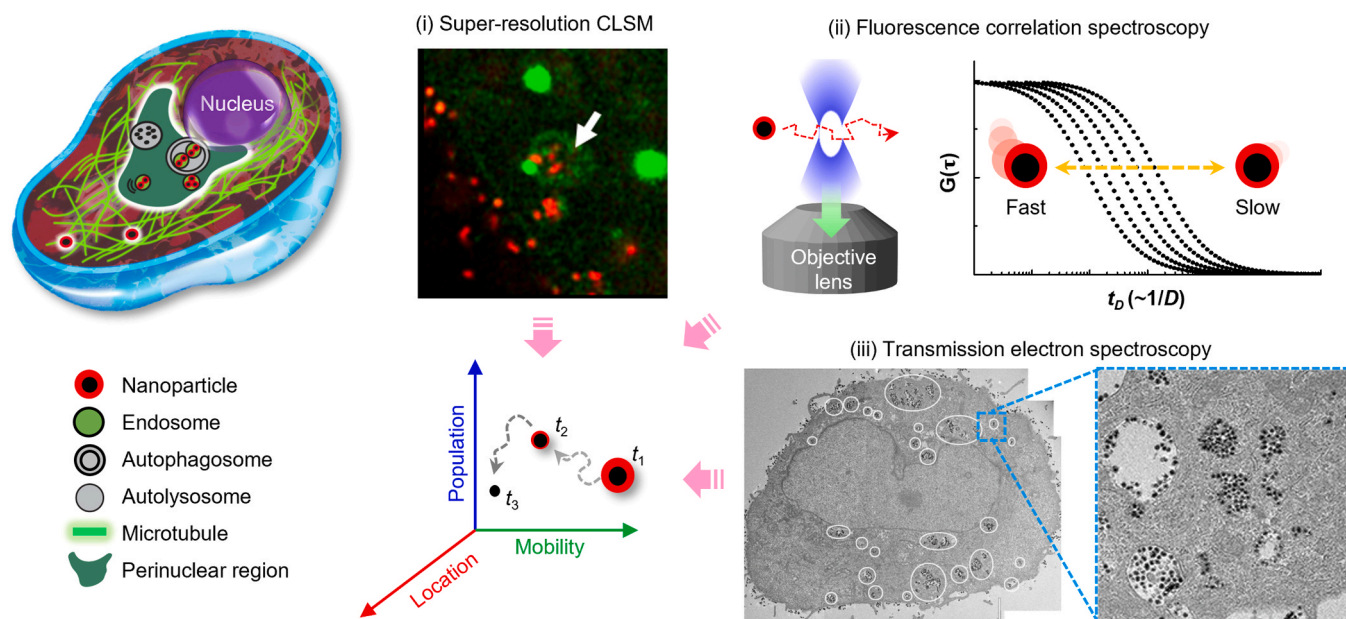
Fig. 1. Schematic workflow of complementary imaging analysis that reveals intracellular trafficking of the nanoparticles through (i) super-resolution confocal laser scanning microscopy (CLSM), (ii) fluorescence correlation spectroscopy (FCS), and (iii) transmission electron microscopy (TEM) in sequential order. Note that the nanoparticles (red) and autophagy stimulation (GFP-LC3, green) were confirmed by CLSM, while dynamic motion of individual intracellular nanoparticle was quantitatively analyzed by FCS, followed by investigating the nanoparticle population and location along with cellular organelles via TEM in sequential order.

while exhibiting strong fluorescent emission (Fig. 1D). In addition, it has been known that maximal cellular uptake of silica nanoparticles is achieved at a diameter of ~50 nm [46], thus we use the $Fe_3O_4@SiO_2$ nanoparticles with a comparable size (~ 55 nm) as a model probe to investigate intracellular mobility and trafficking in this study.

Since hydrodynamic characteristics of the nanoparticles provide key features on intracellular transport, the FCS analysis allows to investigate the quantitative evaluation of intracellular distribution and mobility of the nanoparticles. Fluorescence autocorrelation functions obtained by FCS are typically fitted in a two-component diffusion model to remove photochemical effects, such as blinking (fast fluorescence decay) caused by the rapid diffusional mobility of cellular components [47]. However, those obtained from the nanoparticles immersed in phosphate-buffered saline (PBS) are assumed to fit a one-component free diffusion model (Fig. 2E). It should be noted that the $Fe_3O_4@SiO_2$ nanoparticles in the cytosol show less diffusional motion than that obtained in PBS, indicating restrained diffusion in the cells, possibly due to cellular viscosity and/or confined states of the nanoparticles within the endosomes (Fig. 2E and Table 1) [48]. Moreover, the hydrodynamic property of $Fe_3O_4@SiO_2$ nanoparticles are well matched to those of the bare fluorescent SiO_2 nanoparticles (same size, but absence of magnetic core) in PBS, indicating comparable intracellular dynamics despite the presence of iron oxide core. Besides, surface chemistry such as ionic charge and functional groups is one of the crucial factors that determine the cellular uptake and intracellular behavior of nanoparticles. The zeta potential is −31.5 mV and −34.1 mV for the $Fe_3O_4@SiO_2$ and the bare fluorescent SiO_2 nanoparticles, respectively, supporting comparable hydrodynamic motion in the intracellular trafficking. Overall, the results demonstrate that the $Fe_3O_4@SiO_2$ nanoparticles have comparable intracellular dynamic motion to the SiO_2 nanoparticles in live cells; thus, they are suitable for high-contrast TEM analysis as complementary imaging probes, replacing common silica-based drug delivery carriers such as mesoporous silica nanoparticles suffering from less visibility.

We further investigated the effect of functional groups on the nanoparticle surface as it critically contributes on physiological stability, cellular internalization, and toxicity of the nanoparticles (hence, modulates their biological fate) [49–51]. Among the biologically relevant functionalization including polyethylene glycol (PEG), amine

(-NH₂), carboxyl (-COOH), and hydroxyl (-OH) groups, amine-functionalized nanoparticles show rapid and vast uptake and continuously accumulated in intracellular compartments, particularly in lysosomes (Fig. 2F-H). Lysosomal accumulation indicates that endocytosis is a major pathway in cellular uptake of the $Fe_3O_4@SiO_2$ nanoparticles (Fig. 2I), while cumulative amounts and kinetics depend on the type of surface chemistry. As negatively charged characteristics of phospholipids on the cell membrane are suitable to attract positively charged nanoparticles followed by rapid and higher uptake, we then focus on the amine-functionalized $Fe_3O_4@SiO_2$ nanoparticles and their intracellular trafficking in the present study at a single cell level.

Complementary imaging analysis of intracellular nanoparticle trafficking

To clarify the intracellular trafficking of nanoparticles during endocytosis, we used the complementary imaging systems as suggested above. In the early stage of incubation (~2 hr), the nanoparticles tend to be evenly distributed in the cytosol, then gradually accumulate at the perinuclear region in the later stages (Fig. 3A-D). Corresponding FCS analysis shows time-dependent diffusional mobility of the nanoparticles in the cytosol to be directly related to the hydrodynamic size distribution (Fig. 3E-G) [52]. Since the cytosolic viscosity of HeLa cells is four-fold greater than that of water [47], the diffusion coefficient of the nanoparticles in the cytosol, which ranges from 0.1 to 1.0 μm²/s, corresponds to the hydrodynamic diameter ranging from 600 to 60 nm, respectively (see also *Materials and* m*ethods* section). Therefore, the diffusion coefficient measured at ~1 μm²/s indicates the presence of freely moving single nanoparticles (~ 60 nm in hydrodynamic diameter) in the cytosol. A gradual shift to the shorter diffusion coefficient in the later stages of endocytosis indicates a decelerating diffusion phenomenon, potentially due to either an increased vesicle population (endosomes or lysosomes) that traps the nanoparticles or aggregation of each nanoparticle in the cytosol. Overall, combinatorial study of intracellular nanoparticle diffusion using fluorescence-assisted analysis using CLSM and FCS provided localization and hydrodynamic motion of the nanoparticles, respectively. Hydrodynamic size distribution and diffusional mobility of nanoparticles in the cell can further provide information on intracellular location and dispersion in terms of whether they are freely
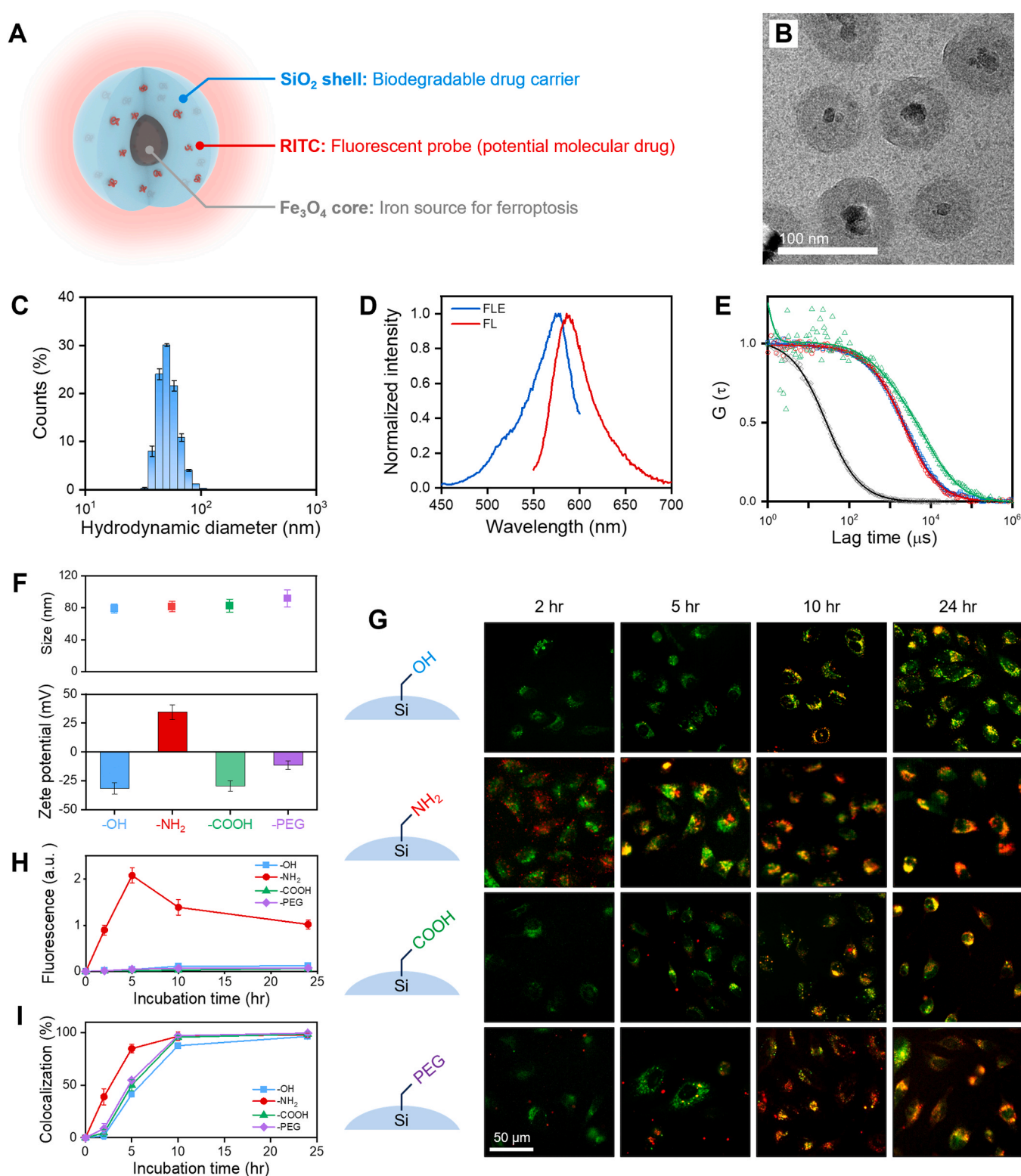
Fig. 2. Physicochemical characterization of Fe3O4@SiO2 nanoparticles for cellular uptake and imaging. (A) Schematic illustration depicting the core@shell structure of a nanoparticle. Note that RITC molecules are embedded in SiO2 shell as a potential drug payloads which also allows fluorescene imaging. (B) Transmission electron microscopy imaging and (C) hydrodynamic size distribution of the nanoparticles. (D) Fluorescence (FL) and fluorescence excitation (FLE) spectra of emission obtained with $\lambda_{ex}=520$ and $\lambda_{em}=620$ nm, respectively. (E) Normalized fluorescence autocorrelation functions, G (τ), of bare RITC (10^{-7} M in PBS, black), SiO2 nanoparticles (10^{-9} M in PBS, blue), Fe3O4@SiO2 nanoparticles (10^{-9} M in PBS, red), and Fe3O4@SiO2 nanoparticles (10^{-9} M in cytosol, green). Note that RITC was embedded in SiO2 for both nanoparticles. Fluorescence autocorrelation functions were fit to the theoretical model (solid lines) of diffusional motions (see also the Materials and methods section). (F) Mean hydrodynamic size and zeta potential of nanoparticles after surface modification as indicated. (G) Fluorescence microscopy images showing intracellular uptake of nanoparticles in HeLa cells upon treatment with nanoparticles containing different surface chemistry. Incremental uptake of nanoparticles (red) and their cumulative overlap with lysosomes (green, LysoTracker) for an extended period of incubation is further quantitatively analyzed by measuring cumulative FL intensity of nanoparticles in cells (H) and by examining colocalization of nanoparticle in lysosomes (I).

Table 1

Hydrodynamic size, diffusion coefficient, and zeta potential of the nanoparticles.

Imaging probe	Diffusion coefficient ($\mu m^2/s$)[a]	Hydrodynamic diameter (nm)[b]	Zeta potential (mV)[c]
Rh6G	280	-	-
SiO₂ (PBS)	4.1±0.4	62	-34.1
Fe₃O₄@SiO₂ (PBS)	4.0±0.3	62	-31.5
Fe₃O₄@SiO₂ (cytosol)	0.9±0.3	64	-

[a] Diffusion coefficient was calculated from the fitted curve and the standard value of Rh6G.

[b] Hydrodynamic diameter was obtained by FCS using Stokes-Einstein equation (see Experimental section).

[c] Zeta potential was determined by using Zetasizer Nano ZS (Malvern, UK).

diffusing as an individual nanoparticle or in mobile phase as vesicle-entrapped nanoparticle complexes. Although the results suggest the existence of cytosolic single nanoparticles along with vesicle-confined nanoparticles, the diffusional behavior related to interactions with cellular organelles in the intracellular trafficking process should also be further confirmed in detail. In this regard, we continue to investigate the intracellular localization of the nanoparticles at an ultrastructural level using TEM.

Upon exposure to nanoparticles, cells are readily surrounded by nanoparticles through the electrostatic interaction between cationic nanoparticles and negatively charged plasma membrane (Fig. S1). It should be also noted that the plasma membrane forms ruffles of different shapes and engulfs a large amount of extracellular membrane-bound nanoparticles (Fig. S2), followed by creating macropinosomes, thus nonspecifically encapsulates the nanoparticles and induces

macropinocytosis as another route of intracellular transport of the nanoparticles [53–55]. However, most of nanoparticles are trapped in endosomes, which exist as a nearly monodisperse form in the cytosol at 2 hr of incubation (Fig. 3H), and then, groups of multiple adjacent endosomes are gradually fused to form larger vesicles at an extended period of incubation (Fig. 3I-L). As a result, the nanoparticles are much frequently found in very large endosomes (> 500 nm) or lysosome-like structures at 5 hr. Furthermore, higher degree of clustering in the lysosomes is observed at 10 hr (Fig. 3J and Fig. S3). Correspondingly, the average number of nanoparticles in each endosomal vesicle significantly increases over time (Fig. 3M), indicating the time-dependent accumulation of clustered or enlarged endosomes in the perinuclear region, which is consistent with CLSM analysis (Fig. 3B-D). Since the nanoparticle-containing vesicles show no evidence of co-localization with Golgi complexes, the cellular organelles located near the perinuclear region, the nanoparticles are trapped in the vesicles and transported to the perinuclear region rather than independently interacting with other cellular organelles such as Golgi apparatus (Fig. S4). Overall, the results suggest that both endosome-trapped nanoparticles and freely diffusing single nanoparticles gradually join to form larger endosomes, and eventually lysosomes, over time. We speculate that continuous accumulation of nanoparticles in an endosome may cause endosomal fusion and enlargement.

We further demonstrated time-course tracing of the intracellular nanoparticles to investigate the lysosomal accumulation of the endocytic nanoparticle as a course of autophagic clearance. In accordance with above findings, the incremental number of intracellular nanoparticles is observed, followed by tremendous increase of corresponding lysosomal nanoparticles near perinuclear region, indicating the spontaneous transport to lysosomes as a result of endocytosis (Fig. 4A and B). Delayed increment of lysosomal nanoparticles supports serial trafficking
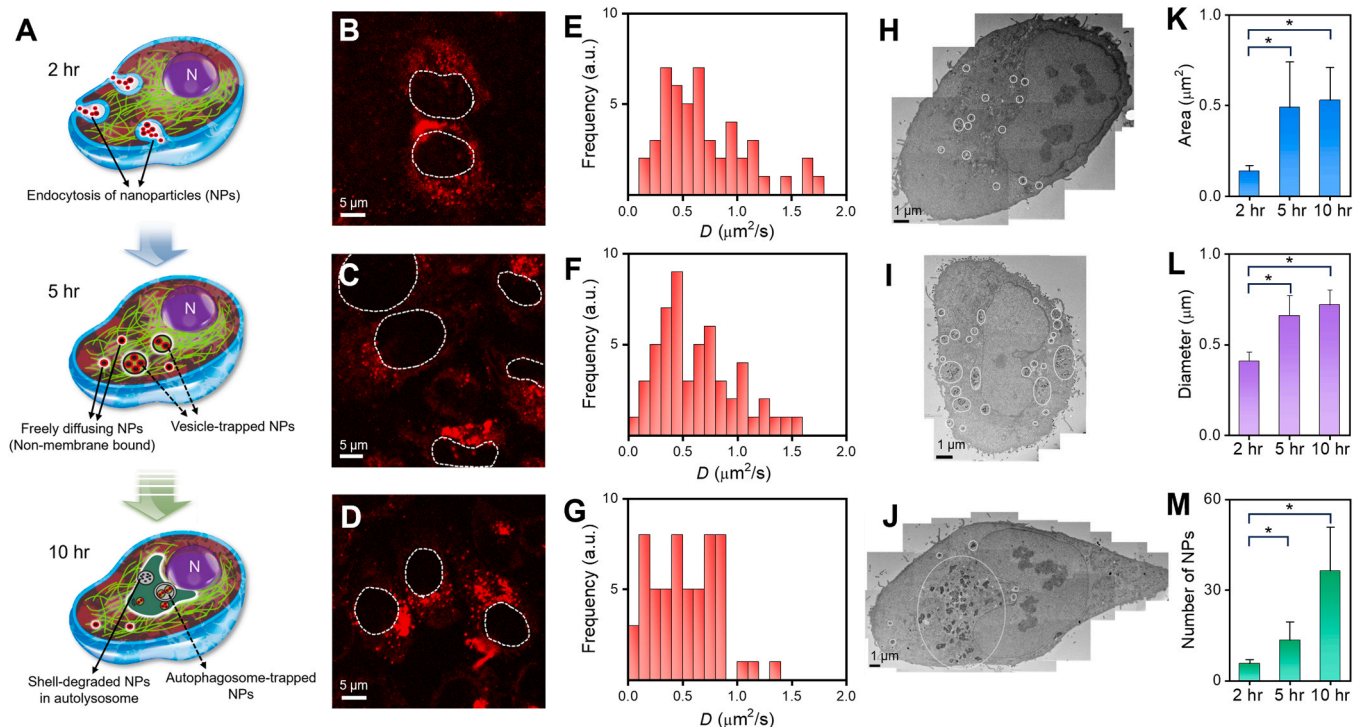

Fig. 3. Intracellular trafficking of endocytic nanoparticles revealed through complementary imaging analysis. (A) Schematic illustrations showing endocytic uptake of nanoparticles, followed by endosomal trafficking and perinuclear accumulation. (B-D) Representative CLSM images of nanoparticles (0.1 mg/mL) in the HeLa cells at 2 h (B), 5 h (C), and 10 h (D) post-incubation. Cell nuclei are indicated by white dashed lines. Scale bar: 5 μm. (E-G) Histogram of the diffusion coefficients (*D*) for nanoparticles in the cytosol obtained at 2 h (E), 5 h (F), and 10 h (G) post-incubation. (H-J) Representative TEM images of HeLa cells obtained at 2 h (H), 5 h (I), and 10 h (J) post-incubation. White circles indicate the endocytosis-related vesicle containing the intracellular nanoparticles. Scale bar: 1 μm. (K) Mean area and (L) diameter of the nanoparticle-trapped endosomes. (M) Corresponding mean number of nanoparticles trapped in a single endosome. Endosomal trapping of nanoparticles was characterized by observation in the inner cell area (n ≥ 5). Error bars show standard error of the mean value (* $p < 0.05$).

of endocytic nanoparticles to lysosomes. Moreover, it should be also noted that lysosomal nanoparticles reach the plateau at 10 hr post-incubation while the intracellular nanoparticles per cell gradually increases (Fig. 4C). The result emphasizes both the degradative feature of the nanoparticles and the transformation of lysosome to autophagosome at the perinuclear region.

Tracing intracellular transport of individual nanoparticles

In the course of endocytosis, most of the nanoparticles is typically located in endosome-originated vesicles during intracellular trafficking. However, we found that a few nanoparticles are presented in a non-membrane-bound form in cytosol (Fig. 5A). These cytosolic nanoparticles are supposed to freely diffuse, thus they are individually distributed. Interestingly, each individual nanoparticle eventually migrates into endosome-like agglomerates over time, resulting in reduced population, although they are not initially trapped in the vesicles (Fig. 5B). Consequently, the complementary imaging analysis strongly supports that the rapid cytosolic diffusional behavior of the individual nanoparticle obtained in FCS (Fig. 3E-G), corresponding to a hydrodynamic size of ~60 nm, is essentially attributed to the freely diffusing, non-membrane-bound individual nanoparticles, as observed in TEM.

Since the cellular uptake of nanoparticles is also induced by applying electrical pulses, we further investigated the diffusional motion of intracellular nanoparticles permeated across the cell membrane via electroporation. Due to the enhanced cell permeability under electrical field, a larger number of nanoparticles are detected as individually distributed forms (freely diffusing nanoparticles) compared to those observed in endocytosis (Fig. 5C and D). Although over half of the intracellular nanoparticles are still found in endosome-like vesicles at 2 hr after electroporation, significantly massive quantity of the cytosolic nanoparticles supports the presence of non-vesicle-trapped

nanoparticles through cellular internalization. In addition, the electroporation of the nanoparticles into the cells leads to maintain the higher diffusion coefficient for much longer time (12 hr) than that of endocytosis (2 hr), indicating the higher degree of the individual nanoparticle uptake than endocytosis (Fig. S5). Because the electroporation physically opens the cell membrane and directly introduces the nanoparticles into the cytosol, it is likely that the cytosol contains a much larger number of non-membrane-bound nanoparticles than endocytic internalization [56]. Complementary imaging analysis clearly reveals the presence of both endosomal and cytosolic nanoparticles as well as their gradual integration during the course of cellular trafficking.

Nanoparticle-induced cellular autophagy

Autophagy is a self-digestive cellular process that delivers cytoplasmic materials of both endogenous and exogenous origin to the lysosome for enzymatic degradation [57]. Although a variety of nanoparticles has been known to lead cellular autophagy, resulting in biodegradation, clearance, or even cell death as a result of toxin release, studies are limited in macroscopic verification [58–60]. However, our complementary imaging analysis extensively presents to validate the cellular autophagy formation at a single nanoparticle level in the course of intracellular trafficking. Upon exposure to the nanoparticles, HeLa cells expressing GFP-LC3 shows elevated level of LC3, which is a central protein in the autophagy pathway where it functions in substrate selection and biogenesis of autophagosomes [61,62]. Cytosolic form of LC3-I undergoes site-specific proteolysis and lipidation on its C-terminus to form LC3-II, thus the punctate green fluorescence emission of GFP-LC3 is correlated with the number of autophagosomes and used as an autophagy marker in the cell [63]. Moreover, intracellular uptake of the nanoparticles stimulates the changes in GFP-LC3 localization, as a number of punctate GFP signals is overlapped with the nanoparticles
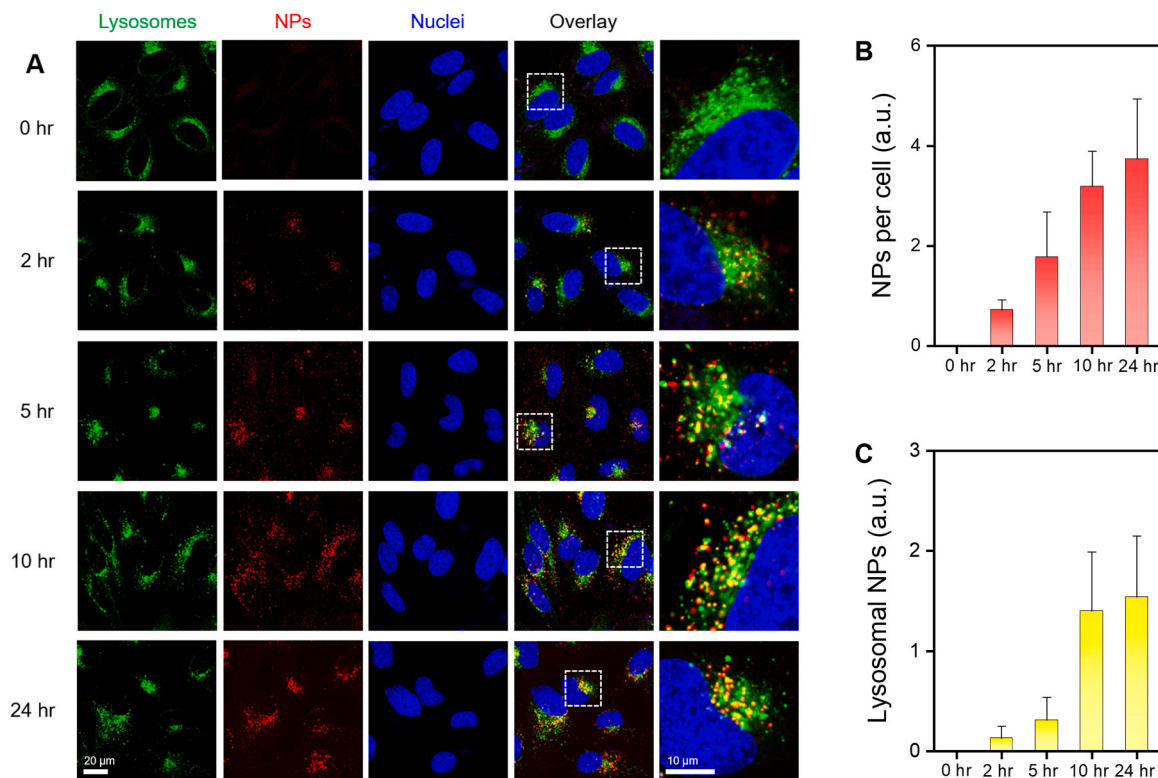

Fig. 4. Accumulation of the nanoparticles in lysosomes near perinuclear region. (A) High-resolution CLSM images show time-course incremental uptake of nanoparticles (red) and cumulative overlap with lysosomes (green: LysoTracker) in the perinuclear region. (B, C) Mean fluorescence intensity of (B) intracellular nanoparticles and (C) lysosomal nanoparticles per single cell (*n*=20) obtained from the CLSM. Note that cumulative lysosomal nanoparticles were quantitatively analyzed through the overlap (yellow) of nanoparticles (red) and lysosomes (green) observed in (A).
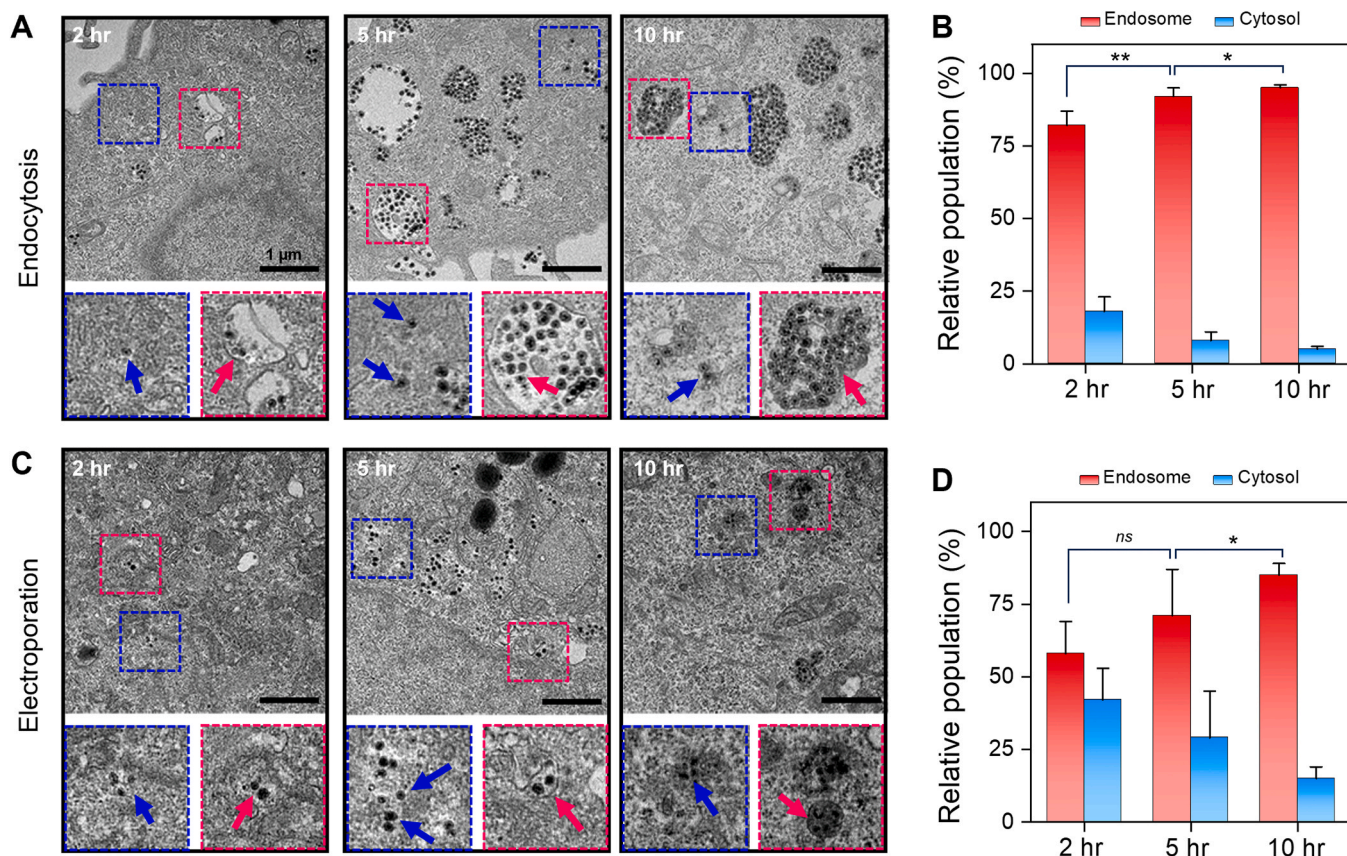
Fig. 5. Distribution of intracellular nanoparticles upon cellular uptake via endocytosis and electroporation. (A) Representative TEM images of HeLa cells treated with the nanoparticles via endocytosis, and (B) relative population of nanoparticles located in endosomes and cytosol as a function of incubation time, respectively. (C) Representative TEM images of HeLa cells treated with the nanoparticles via electroporation, and (D) relative population of nanoparticles located in endosomes and cytosol for a designated period of incubation time. Scale bar: 1 μm. In TEM images. each panel contains enlarged images of the dotted line box at the bottom for clarity. Blue and red arrows represent the cytosolic nanoparticles (non-membrane-bound) and endosome-trapped (endosomal) nanoparticles, respectively. * $p < 0.1$ and ** $p < 0.05$ from the two-tailed Student's t test (*ns*: not significant, $n = 5$).

found in the perinuclear region, while GFP-LC3 usually showed high localization in the nucleus and few spots in the cytosol prior to the introduction of the nanoparticles (Fig. 6A-D).

Corresponding TEM images show the autophagic structures such as double membrane autophagosomes and autolysosomes containing the nanoparticles at 5 hr or later post-uptake (Fig. 6E-H). Particularly, it should be noted that the silica shell surrounding the dark Fe_3O_4 core maintains the structural integrity up to 10 hr (Fig. 6G and I) while only parts of the Fe_3O_4 core without a silica shell are observed in the endolysosomes at 24 hr (Fig. 6H and J). The results indicate the biodegradable clearance of the silica shell and iron oxide core during the intracellular trafficking, particularly in the lysosomes, which corresponds with the above findings (Fig. 4 and Fig. S3). Overall, the complementary imaging analysis using CLSM and TEM consistently supports our findings on cellular trafficking of the nanoparticles and autophagic clearance of the nanoparticle compartments. The present study further emphasizes the biodegradable feature of silica, which is a widely used as a drug delivery carrier, implying complete release of payloads during autophagy process.

In addition to the complementary imaging analysis, the nanoparticle-stimulated autophagy activation is further confirmed through relevant protein assays. Western blots and corresponding densitometry showed time-dependent variation (Fig. 6K and L). In particular, LC3-II expression and the LC3-II/LC3-I ratio are significantly increased upon nanoparticle uptake, which is then returned to intrinsic levels within 24 hr. The result indicates transient induction of LC3-II due to the nanoparticle uptake. Moreover, it confirms that not only autophagosome accumulation of the nanoparticles but also autophagic clearance are consistent

with the complementary imaging tracking. As autophagy is a programmed degradative pathway that plays an essential role in maintaining cellular homeostasis, the foreign substances (i.e., nanoparticles) introduced into the cell are readily degraded by the autophagy mechanism without causing acute cellular disorder, possibly due to the elemental biocompatibility of silica and iron oxide [40,64]. In contrast, gold nanoparticles have been observed to cause the impairment of autophagosome-lysosome fusion and reduced lysosomal degradation capacity with lysosome alkalization [58]. Accordingly, cell viability results verify the non-cytotoxic degradable characteristics of the $Fe_3O_4@SiO_2$ nanoparticles, related to the functional capability for cellular autophagy (Fig. 6M).

Although an influx of highly biocompatible and hydrophilic $Fe_3O_4@SiO_2$ nanoparticles into cells activates the autophagy without severe cytotoxicity even at elevated concentrations (up to 0.2 mg/mL), the individual nanoparticles possibly leaked from vesicles or freely diffused in the cytosol are highly mobile, and thus, potentially accessible to all intracellular organelles. In practice, nanoparticles that have chemically reactive surfaces tend to interact strongly with intracellular organelles, such as mitochondria and actin/tubulin networks, eventually resulting in damage to the cell functions [65]. However, the $Fe_3O_4@SiO_2$ nanoparticles used in this study are chemically inert in a cellular environment, and show minimal interaction with intracellular organelles, such as mitochondria (Fig. S6). Therefore, it can be assumed that those freely diffusing individual nanoparticles are inevitably trapped into autophagosomes with other nanoparticle-containing endosomes and ultimately introduced to lysosomes for intracellular biodegradation without any severe cytotoxic effects. In addition to
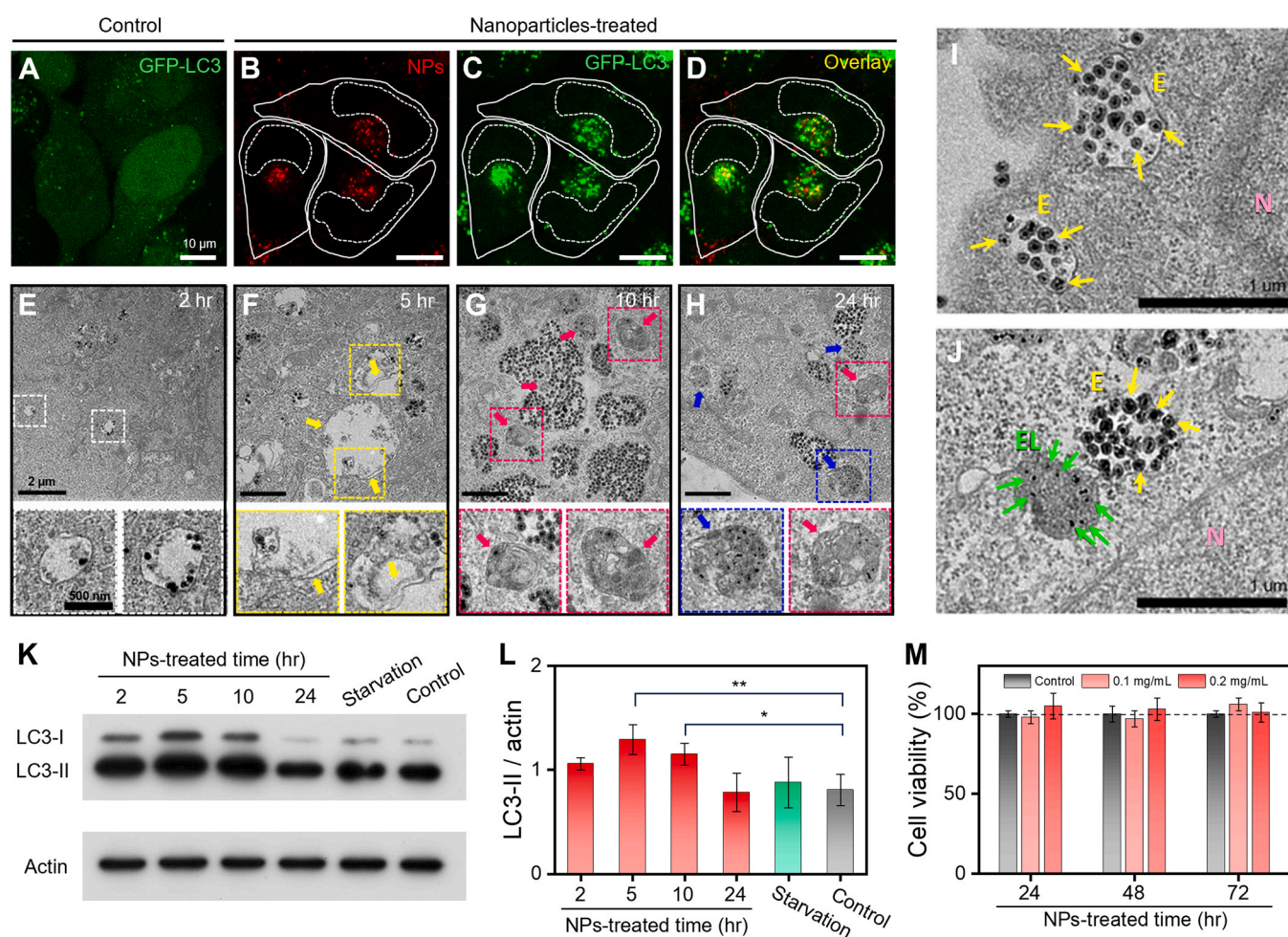
Fig. 6. Autophagy stimulation and nanoparticle uptake. (A) Representative CLSM image of the HeLa cells expressing GFP-LC3, a marker protein for autophagosomes, prior to nanoparticle treatment. (B-D) Corresponding CLSM images of the HeLa cells after treatment with the nanoparticles (red) for 5 h. Remarkable punctate fluorescence emission of GFP-LC3 (green) was detected in the perinuclear region. The cell membrane and nucleus are circumscribed for clarity (white solid lines and dotted lines, respectively). Scale bars: 10 μm. (E-H) TEM images of the nanoparticle-treated HeLa cells at post-uptake for (E) 2 hr, (F) 5 hr, (G) 10 hr, and (H) 24 hr, respectively. Yellow arrows in (F) indicate vacuoles with double-spaced membranes that contain the cell components and nanoparticles. Red and blue arrows in (G) and (H) indicate autolysosomes and lysosomes, respectively. Scale bars: 2 μm. Each panel shows two magnified views of designated regions of interest marked in the dotted box at the bottom. Scale bars: 500 nm. (I) TEM image of the endosome-like structures containing the nanoparticles near the perinuclear region of the HeLa cells at 5 h post-incubation. (J) The nanoparticles trapped in an endolysosome and an endosome at 24 h post-incubation. Green arrows indicate the iron oxide core of the nanoparticles without silica shells due to degradation while yellow arrows designate the intact silica shell (see also (G) and (H)). E: endosome, EL: endolysosome, N: nucleus. Scale bars: 1 μm. (K) Western blot analysis of LC3-I and LC3-II in HeLa cells treated with the nanoparticles (0.1 mg/mL) for 2, 5, 10, and 24 hr. Note that starvation and control (no nanoparticle treatment) samples showed negligible differences in LC3-I expression, and the elevated LC3-I expression upon nanoparticle treatment is recovered by 24 hr. (L) Relative ratio of LC3 II to β-actin (** $p < 0.005$ and * $p < 0.05$). (M) Negligible cell viability changes found upon nanoparticle exposure to the cells showing biocompatible degradation of the nanoparticles by autophagic clearance.

clarify the intracellular trafficking by which the nanoparticles induce autophagosome accumulation and lysosomal degradation, our complementary imaging analysis provides guidance for the rational design and preparation of nanoparticles for diverse areas in biomedical applications, such as targeted drug delivery and bioimaging.

Furthermore, we also verify the co-localization of autophagosomes and nanoparticles using super-resolution CLSM in another cell line, human breast adenocarcinoma MCF7 expressing GFP-CL3. Time-lapse imaging reveals the highly mobile nanoparticles found in a large autophagosome (Fig. S7 and Movie S1) and shows dynamic motion of each nanoparticle while trapped in the confined space. Although it remains unknown whether the fluorescence signal comes from a single nanoparticle or vesicle-constrained multiple nanoparticles due to limited resolution, these results provide evidence of the autophagy activation stimulated by the nanoparticle uptake. Moreover, physical interactions between the highly mobile GFP-LC3 molecules and nanoparticles are not directly observed in the cytosol (Fig. S8).

Supplementary material related to this article can be found online at doi:10.1016/j.nantod.2024.102242.

The complementary imaging analysis combines information on localization (CLSM), hydrodynamic mobility (FCS), and interactions with intracellular organelles (CLSM and TEM), providing a comprehensive view of nanoparticle dynamics during intracellular trafficking. While previous studies have utilized conventional fluorescence imaging alongside TEM [66–68], our approach of cross-verifying information from multiple imaging modalities enhances the reliability and credibility of our findings, offering a more complete understanding of intracellular nanoparticle dynamics. Overall, the integration of super-resolution CLSM, FCS, and TEM (TEM) provides a comprehensive understanding of intracellular nanoparticle dynamics. The super-resolution CLSM offers high spatial resolution for precise visualization of nanoparticles and their interactions with organelles while the FCS quantitatively analyzes nanoparticle mobility and diffusion dynamics within cells, complementing super-resolution microscopy. TEM

contributes a structural perspective, offering high-resolution images of nanoparticles and cellular organelles, facilitating observation of structural changes, interactions, and degradation processes at the nanoscale level. Despite differences in working principles and sample preparation requirements, the complementary imaging system addresses the limitations of each individual imaging modality, enabling a more comprehensive understanding of nanoparticle-cell interactions. This integration enables in-depth analysis of nanoparticle dynamics at the single-cell level, providing valuable insights into nanoparticle uptake, intracellular trafficking, and cellular responses, thus advancing various fields such as nanomedicine, drug delivery, and nanotoxicology.

Delayed degradation of silica shell for protecting iron oxide core

We observed the non-toxic biodegradation of nanoparticles while they induce autophagic clearance. Under normal physiological conditions, the hydrolysis of the silica shell resulted in its spontaneous degradation, releasing silicic acid (as shown in Fig. 7A). To investigate the step-by-step of autophagic clearance, particularly in terms of silica shell degradation, microstructural changes in the morphological characteristics of nanoparticles has been further conducted. Since the biodegradation of the silica shell is closely related with the acidity of the local microenvironment, we measured the degradation kinetics of nanoparticles in cell culture media with adjusted pH. We used RITC molecules as model payloads to mimic drug delivery, and the cumulative release of RITC served as a distinctive indicator of the inherent self-destructive characteristics of the silica shell (Fig. 7B). It should be noted that release kinetics of RITC is strongly dependent on the acidity of the solution. Rapid release of RITC at higher pH indicate accelerated degradation of silica shell, while reduced degradation kinetics at acidic environment imply relatively stable feature of silica by providing oxidational condition rather than hydrolysis. Degradation of silica shell is also confirmed by TEM analysis (Fig. 7C). In neutral condition, silica shell is completely degraded within 24 hr of incubation in cell culture media. However, the nanoparticles maintain the intact structure at acidic environment. The results suggest autophagic degradation of the nanoparticles is also associated with the local acidity during intracellular trafficking. Importantly, the nanoparticles showed slower degradation kinetics in PBS compared to that of cell culture media (Fig. S9). Since the intracellular vesicles are known to have weak acidic environment ($\sim$ pH 6.5 for endosome, $\sim$ pH 4.5 for lysosomes, etc.), degradation of silica shell is strongly associated with autophagic clearance. Perhaps, silica shell is continuously degraded during the course of endocytosis, thus iron oxide nanoparticles are exposed to physiological environment at the later stage such as in lysosomes or endolysosomes.

Inspired by protective feature of silica shell during intracellular trafficking, we can further utilize the iron oxide nanoparticles as an iron source for inducing ferroptosis. Ferroptosis is a form of regulated cell death that is characterized by the iron-dependent accumulation of lipid peroxides, which ultimately leads to the destruction of cell membranes and cell death [69]. Although degradation of iron oxide nanoparticles in acidic lysosomes or autophagosomes may contribute to oxidative stress, this effect is negligible for cell viability (Fig. 6M). However, among two products of iron oxide dissolution, converting ferric ions (Fe^{3+}) to ferrous ions (Fe^{2+}) can be a key to induce ferroptosis. Because ferrous ions promote ferroptosis by catalyzing the formation of reactive oxygen species (ROS) and lipid peroxides, while ferric ions have an inhibitory role by countering these pro-oxidant effects and protecting cells from oxidative damage [70]. To convert the ferric ions to ferrous ions, we used ascorbic acid as a reductant (Fig. 7D). The level of ferrous ions in the media during the process of nanoparticle degradation is substantially increased by adding ascorbic acid (Fig. 7E and F). Particularly, weak acidic condition (pH ~6.5) is more feasible to produce ferrous ions as it helps to degrade the silica shell after 5 hr of incubation and also leads ionic dissolution of iron oxide nanoparticles. Although acidic environment is well suited to ironic dissolution of iron oxide, the silica

shell is protecting the iron oxide core until 24 hr at pH $\sim$ 5.5 or $\sim$ 4.5, resulting in significantly lower levels of ferrous ions even after the introduction of ascorbic acid. Therefore, delayed degradation of silica shell is an attractive feature for burst release of ferrous ions associated with cellular trafficking of nanoparticles.

Triggered ferroptosis upon burst release of ferrous ions

In the context of ferroptosis, the elevation of ferrous ions assumes a pivotal role in driving this regulated cell death process. Since the ferroptosis is characterized by the iron-dependent accumulation of lipid peroxides and subsequent cell membrane disruption, it hinges on the pro-oxidant properties of ferrous ions. These ions serve as catalysts in the Fenton reaction, a chemical process that couples ferrous ions with hydrogen peroxide (H_2O_2) to generate highly reactive hydroxyl radicals ($\cdot$OH) and hydroxide ions (OH^-). The hydroxyl radicals, in turn, initiate lipid peroxidation, resulting in membrane damage and increased permeability. This cumulative effect ultimately culminates in ferroptotic cell death. To this end, we propose the acute ferroptosis as a means of triggered cell death upon burst release of ferrous ions resulting from prompt reduction reaction of ferric ions. While individual treatments with ascorbic acid up to 300 μM or nanoparticles up to 200 μg/mL showed negligible cytotoxicity, significant cell death occurred with elevated concentrations of nanoparticles in the presence of ascorbic acid (Fig. S11). This effect was attributed to the rapid reduction of ferric ions to ferrous ions by ascorbic acid, leading to the generation of highly reactive hydroxyl radicals and other reactive oxygen species (Fig. 8A). At certain conditions, cells were able to mitigate oxidative stress through antioxidant pathways, but overwhelming oxidative stress, induced by higher concentrations of nanoparticles (> 50 μg/mL) and ascorbic acid (300 μM), led to ferroptotic cell death. This was evidenced by significant cell death observed in the presence of both nanoparticles and ascorbic acid, potentially resulting from the burst reduction of ferric ions to ferrous ions. Although the nanoparticles are apparently non-toxic in their autophagic clearance pathway and ascorbic acid is not intrinsically harmful to cells, burst reduction of ferric ions to ferrous ions may instantly trigger the ferroptosis (Fig. 8A). In fact, we observed acute cell death by treating with nanoparticle and ascorbic acid (Fig. 8B and Fig. S10). To verify whether ferroptosis is responsible to cell death, an iron-chelating agent, deferoxamine (DFO), was added to the cell treated with both nanoparticles and ascorbic acid. The DFO works to sequester and remove excess ferrous ions in the cell through iron chelation and ROS reduction, followed by protecting cells from the oxidative damage that drives ferroptosis. Therapeutic capability of DFO in conditions where ferroptosis is implicated supports our findings on acute cell death triggered by burst release of ferrous ions. It should be also noted that hydrogen peroxide (H_2O_2) can contribute to ferroptosis-based cell death by serving as a source of ROS. We also showed that elevated lipid peroxide levels in the cell as evidence of ferroptosis (Fig. 8C). The lipid peroxides accumulate within the cell, leading to membrane destabilization, loss of membrane integrity, and ultimately cell death, correspondingly (Fig. 8B and C). Combinational effect of ascorbic acid and hydrogen peroxide with nanoparticles can be considered as a means of triggered acute ferroptosis.

Gradual degradation of silica shell is temporally protecting the iron supplement, which is initiated upon complete removal of silica at late stage of endocytosis. Acidic environment is feasible for iron ion dissolution in forms of Fe^{3+} and Fe^{2+}, and ascorbic acid further induces burst reduction of Fe^{3+} ions to Fe^{2+} ions, followed by acute ferroptosis (Fig. 8D). The results imply that certain critical concentration of Fe^{2+} ions is necessary to induce ferroptosis, otherwise the cells can internally compensate for balancing the iron supplement to maintain the homeostasis. Furthermore, we also found that exposure to ascorbic acid at 10 h or earlier post-incubation of nanoparticles showed no cytotoxicity while ascorbic acid showed effective cell death by injecting at 24 h post-incubation of nanoparticles (Figure S12). The results suggested that
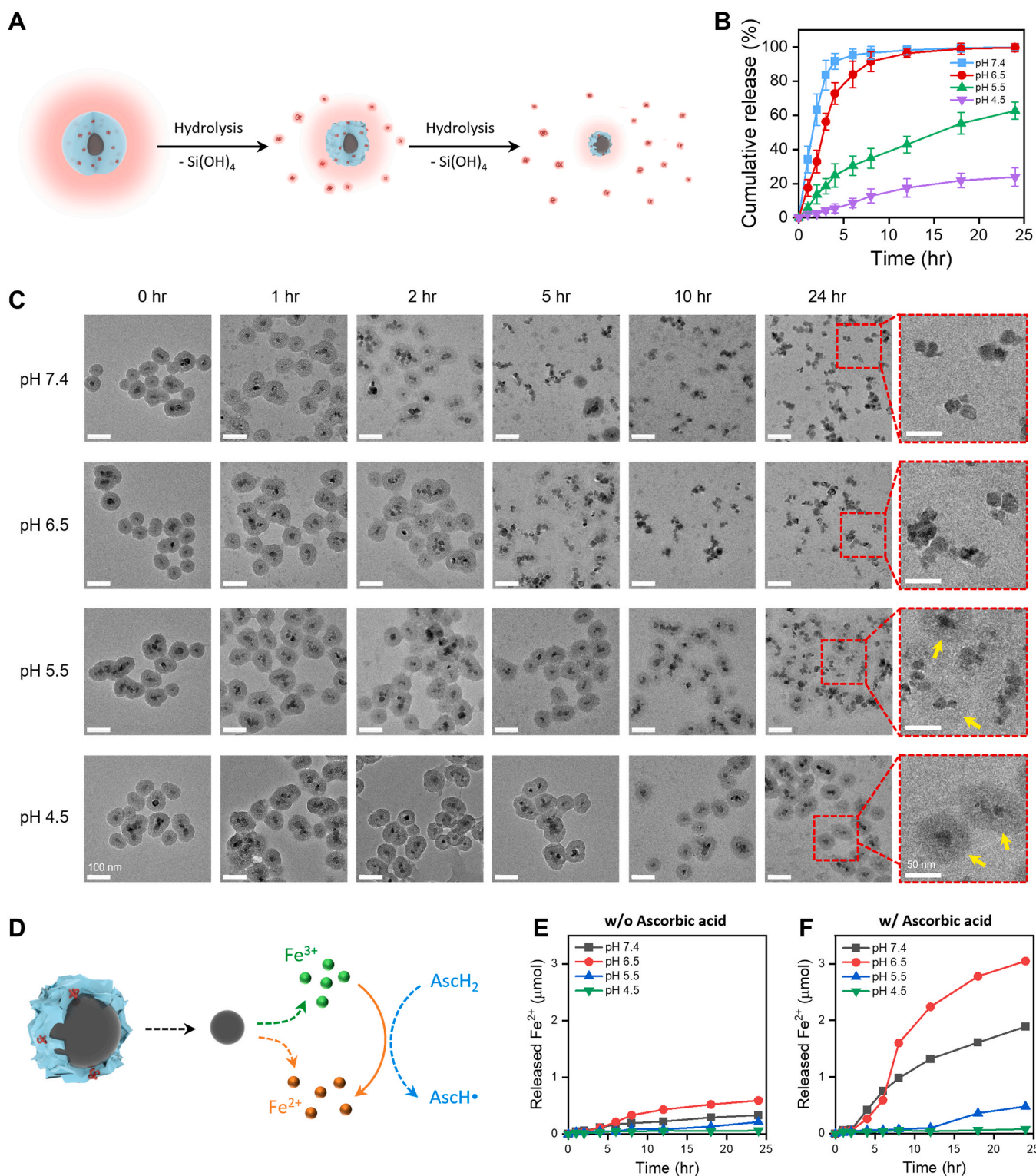
Fig. 7. Biodegradation of nanoparticles and Fe^{2+} production. (A) Schematics illustrating hydrolysis-driven degradation of silica shell in physiological condition. (B) Cumulative release curves of RITC upon incubation in cell culture media with adjusted pH as indicated at 37 °C. (C) Corresponding TEM images of nanoparticles during biodegradation process in designated pH. Yellow arrows indicate the intact silica shell. Scale bar: 100 nm. (D) Schematics depicting the dissolution of Fe^{3+} ions and Fe^{2+} ions resulting from biodegradation of iron oxide nanoparticles. Note that both Fe^{3+} ions and Fe^{2+} ions are released, and ascorbic acid readily leads to reduce Fe^{3+} ions to form Fe^{2+} ions. (E, F) Cumulative amount of Fe^{2+} ions released from the nanoparticles upon biodegradation with (E) absence and (F) presence of ascorbic acid as a reducing agent.
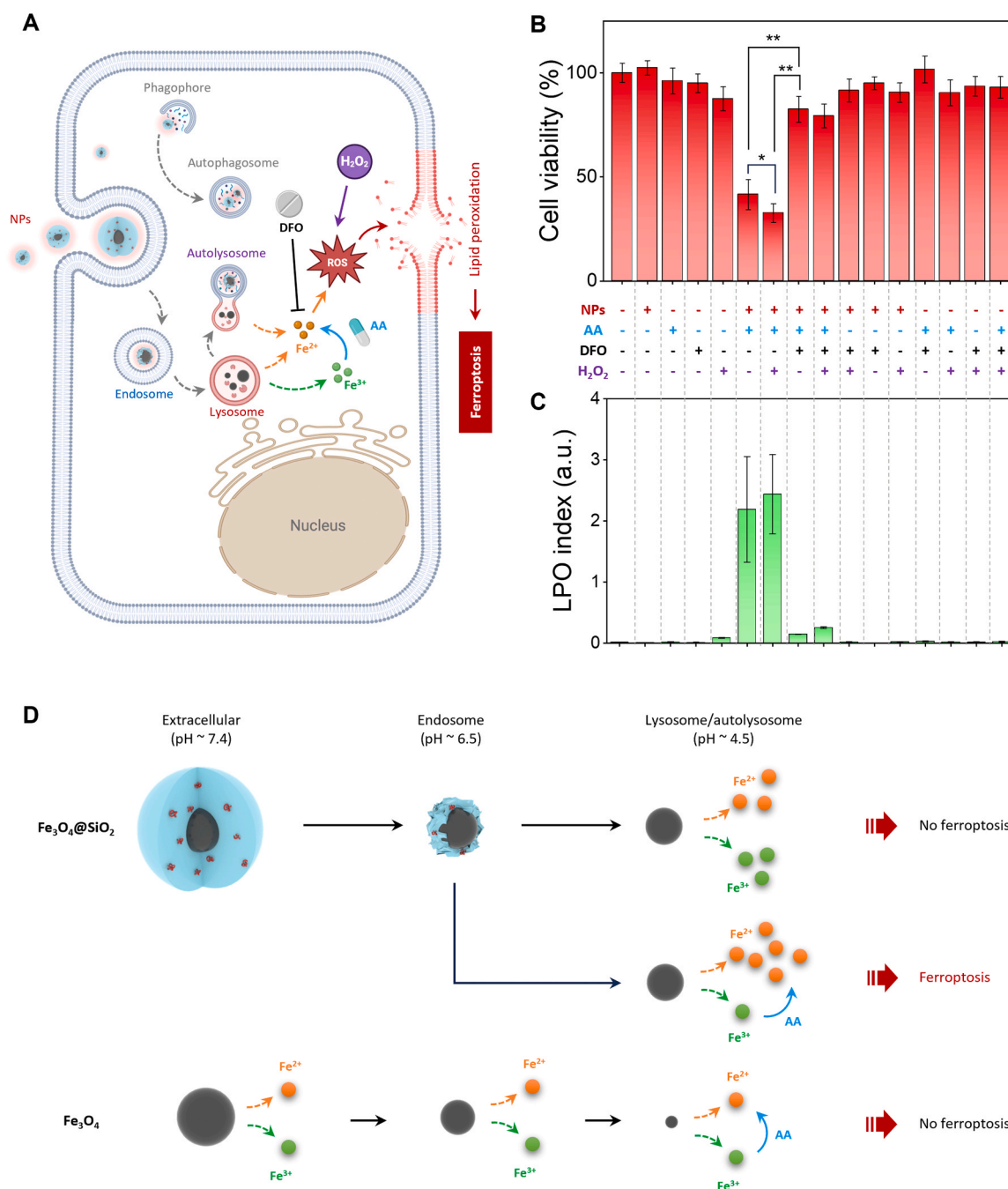
Fig. 8. Acute ferroptosis triggered by burst release of Fe^{2+} ions. (A) Schematic illustrations showing proposed mechanism for the intracellular trafficking of nanoparticles and autophagic clearance. The silica shell is gradually degraded during intracellular trafficking, and iron oxide core could release Fe^{3+} and(or) Fe^{2+} ions in acidic lysosomes. Elevated amount of Fe^{2+} ions resulting from iron oxide nanoparticle degradation does not cause severe toxicity in the cell. However, burst release of excess Fe^{2+} ions led by ascorbic acid-driven chemical reduction of Fe^{3+} ion causes lipid peroxidation by participating Fenton reaction, followed by acute ferroptosis. Ascorbic acid can be used to concentrate Fe^{2+} ions by rapidly reducing excessive Fe^{3+} ion to promote ROS production, meanwhile iron chelating agent deferoxamine (DFO) can inhibit Fe^{2+} formation. (B) HeLa cell viability and (C) lipid peroxidation (LPO) index upon treatment with absence or presence of nano-particles (NPs, 100 ug/mL), ascorbic acid (AA, 300 μM), deferoxamine (DFO, 50 μM), and H_2O_2 (20 μM). (* $p < 0.01$, ** $p < 0.001$) (D) Schematic illustrations summarizing the triggered ferroptosis of $Fe_3O_4@SiO_2$ nanoparticles with addition of ascorbic acid. Note that burst reduction of Fe^{3+} ions to Fe^{2+} ions upon ascorbic acid addition at late stage of endocytic trafficking is only responsible to ferroptosis while gradual release of Fe^{2+} ions are readily neutralized and negligible to induce the ferroptosis.

the ascorbic acid contributed the cell death only if the iron oxide nanoparticles were exposed to intracellular environment after complete degradation of silica shell around themselves. On the other hand, bare iron oxide nanoparticles without silica shell are continuously degraded during intracellular trafficking, thus ionic iron components in the cell may not exceed the critical concentration to induce ferroptosis even

after ascorbic acid treatment. The silica shell is temporally protecting the iron source (nanoparticles) to spatially trigger the ferroptosis by adding the reducing agent (ascorbic acid). Our findings suggest that timely treatment of cells with nanoparticles and reducing agent is a means of controllable cell death. Spatiotemporal tracking of intracel-lular nanoparticles reveals not only the location of transport but also

self-destructive features, leading the triggered ferroptosis mechanism initiated by burst release of ferrous irons.

Discussion

Upon exposure to the nanoparticles, the majority of attractive nanoparticles are allowed to internalize through endocytosis, where small vesicles contain them and further transform to larger vesicles. Correlative imaging of TEM and CLSM highlights (i) the temporal development of the endosomal vesicles, (ii) the intracellular trasport to the perinuclear region, and (iii) the biodegradation of nanoparticle through autophagy process. In addition, combinatorial analysis of FCS and TEM reveals not only the presence of cytosolic (non-vesicle-trapped) nanoparticles but also their Brownian diffusion motion. Comparing the ratio of cytosolic nanoparticles to endosomal nanoparticles supports the intracellular trafficking feature such as cluster formation and incorporation into endosomes. Therefore, the complementary imaging analysis could aid in the design of efficient intracellular delivery systems for therapeutic purposes.

Considering the intracellular motion of the biodegradable Fe$_3$O$_4$@SiO$_2$ nanoparticles in the cytosol, it has been classified by two diffusional behavior: fast diffusion of untrapped nanoparticles (mean D value ~1 μm^2/s) and much slower diffusion of mobile vesicle-trapped nanoparticles (mean D value < 1 μm^2/s). Complementary imaging analysis reveals that a significant proportion of the intracellular nanoparticles initially show fast diffusion, corresponding to the freely moving single nanoparticles with a hydrodynamic diameter of ~60 nm (Fig. 2). However, over the extended period of intracellular trafficking, the nanoparticles gradually form clusters, thus the size distribution broadens, accompanied by slower diffusional movement. These results indicate a reduced number of freely diffusing cytosolic (non-vesicle-trapped) individual nanoparticles in the cytosol at later stages of endocytosis. Therefore, the present study emphasizes the importance of endosomal escape of vesicle-trapped nanoparticles or individual nanoparticle internalization for cytosolic drug delivery. Since the endocytosis is a main mechanism of spontaneous cellular internalization for non-viral vectors including nanoparticles, potential therapeutic payloads such as siRNA or ribonucleoproteins (Cas9/gRNA complexes) should be securely protected and safely released into the cytosol while avoiding enzymatic degradation in the endosomal vesicles [71–74]. Our complementary imaging analysis evidently reveals the spontaneous merging and clustering of the endocytic nanoparticles, followed by the degradation through autophagy process. Besides, we further demonstrated the use of electroporation to internalize the nanoparticles directly to cytosol and showed that a substantial portion of individual nanoparticles are freely diffusing in the cytosol particularly at the early stages of uptake (Fig. 5). The result is responsible for the electroporation as an efficient means of gene delivery into the cytosol [75–77].

The cellular uptake, trafficking, and clearance pathways of nanoparticles, along with their interactions with cellular organelles, have attracted significant attention because these processes need to be well-understood for further translation in biomedical applications. Although a variety of functional nanoparticles have shown excellent proof-of-concepts in performance and been suggested as potential platforms for drug delivery systems and therapeutic agents, only a few have been approved for clinical use or are under consideration for clinical trials due to cytotoxicity that outweighs their therapeutic capabilities. For instance, silica is a biocompatible and biodegradable material, but has also been shown to cause unwanted side effects, such as apoptosis or necrosis, under certain conditions [78]. Therefore, a better understanding of nanoparticle-induced cytotoxicity could be gained by elucidating, in depth, their metabolism within cells. Recent studies have aimed to investigate the interactions of nanoparticles with cells, demonstrating cytotoxic cellular pathways that induce apoptosis and autophagy. In particular, the interaction of nanoparticles with autophagy has been assumed to be responsible for the intracellular clearance pathway, as demonstrated by fluorescence microscopic studies [29,58, 79]. However, the underlying mechanisms still remain unclear. In the present study, thanks to complementary imaging analyses with CLSM, FCS, and TEM, we provide strong evidence that autophagosomes co-localize with the Fe$_3$O$_4$@SiO$_2$ nanoparticles in cells. Moreover, the nanoparticles are observed to be co-localized with autophagosomes at the very late stage of endocytosis. Time-lapse super-resolution CLSM has suggested that both vesicle-trapped and freely diffusing individual nanoparticles are ultimately integrated into autophagosomes, followed by intracellular clearance. Increased levels of LC3-II further support the contention that the nanoparticles induce autophagy, even though the molecular mechanisms of autophagic stimulation and clearance without significant cytotoxicity need to be investigated further. Our combinatorial imaging strategy also indicates the negligible interactions between the Fe$_3$O$_4$@SiO$_2$ nanoparticles and other intracellular organelles, such as mitochondria and Golgi complexes, in the course of endocytosis and autophagic degradation.

While TEM and FCS provides comprehensive information on nanoparticle trafficking and interactions with intracellular organelles, time-lapse super-resolution CLSM enables dynamic visualization of nanoparticle in their cellular context without the need for sample fixation and processing. Notably, CLSM has revealed perinuclear accumulation upon lysosomal degradation and autophagic clearance, aligning with observations from FCS and TEM. Furthermore, time-lapse imaging has captured highly mobile nanoparticles trapped within large autophagosomes. By providing real-time spatiotemporal information, CLSM enhances our understanding of immediate nanoparticle-cellular organelle interactions, complementing the static information obtained from TEM. Additionally, CLSM serves as an independent technique to validate observations from FCS and TEM, thereby enhancing the reliability and robustness of our findings. The combination of CLSM, FCS, and TEM allows for correlative imaging, facilitating a comprehensive analysis of intracellular nanoparticle trafficking and reinforcing the importance of utilizing confocal microscopy for elucidating nanoparticle dynamics within living cells. Particularly, FCS adds a quantitative dimension by elucidating the mobility and diffusion dynamics of nanoparticles within the cellular microenvironment, complementing qualitative observations from CLSM imaging and ultrastructural details from TEM. The diffusion coefficients obtained by FCS clarify the localization of nanoparticles within cellular vesicles, such as lysosomes and autophagosomes, enhancing our understanding of intracellular trafficking. The complementary imaging analysis combines information on localization (CLSM), hydrodynamic mobility (FCS), and interactions with intracellular organelles (CLSM and TEM), providing a comprehensive view of nanoparticle dynamics during intracellular trafficking. Overall, the complementary imaging systems will provide essential analytical information on autophagic clearance and the potential cytotoxicity of various functional nanoparticles with a desired size, shape, and surface chemistry for biomedical purposes.

Ferroptosis represents a significant mode of cell death with relevance to a wide range of diseases and biological process [80]. Particularly, inducing ferroptosis in cancer cells has emerged as a potential strategy for cancer therapy as some cancer cells are highly vulnerable to ferroptosis due to their increased iron uptake and sensitivity to oxidative stress [81]. However, regulation of iron uptake is subject to sophisticated control mechanisms at the molecular and cellular levels. Dysregulation of these mechanisms can lead to iron-related disorders, such as iron-deficiency anemia or iron overload disorders like hemochromatosis. Therefore, while controlling iron uptake is challenging, it is essential for maintaining overall health and preventing iron-related diseases. In our findings using complementary imaging techniques, we propose controllable ferroptosis as a means of cancer treatment. Although both Fe$_3$O$_4$@SiO$_2$ nanoparticles and ascorbic acid are biocompatible, timely treatments can acute ferroptosis for selective cell death. The demonstration of acute ferroptosis underscores the crucial role of ascorbic acid in triggering this form of regulated cell death, particularly when

combined with nanoparticles. Despite the individual treatments with ascorbic acid up to 300 μM or nanoparticles up to 200 μg/mL showing negligible cytotoxicity, a significant increase in cell death was observed with elevated concentrations of nanoparticles in the presence of ascorbic acid. This heightened cytotoxic effect can be attributed to the specific action of ascorbic acid, which rapidly reduces ferric ions to ferrous ions upon addition, thus facilitating the generation of highly reactive hydroxyl radicals and reactive oxygen species. Timely co-treatment illustrates how the burst reduction of ferric ions to ferrous ions by ascorbic acid plays a pivotal role in the induction of ferroptosis. This process is especially significant considering the later stages of cellular vesicles, such as lysosomes and autolysosomes, where iron oxide nanoparticles are readily degraded under acidic conditions, resulting in the release of ionic dissolution products, including Fe^{2+} and Fe^{3+}. By injecting a sufficient amount of ascorbic acid into the cells, the rapid and substantial reduction of ferric ions occurs, triggering a cascade of events culminating in ferroptosis and eventual cell death. While cells possess intrinsic antioxidant pathways and repair mechanisms to counteract oxidative stress under normal conditions, the overwhelming oxidative stress induced by the combined presence of nanoparticles and ascorbic acid exceeds the cellular defense mechanisms, leading to ferroptotic cell death. In addition, the degradation of silica shell was not substantially affected by adding ascorbic acid (Figure S13), as the silica is quite stable in acidic condition. Overall, this experimental evidence highlights the critical interplay between ascorbic acid-mediated reduction of ferric ions and the subsequent initiation of ferroptosis, shedding light on potential therapeutic avenues targeting this pathway for various applications in cellular biology and disease intervention. Although certain mechanisms beyond the triggered ferroptosis might be further existed, the present work reports the findings of potentially triggerable ferroptosis, revealed by a complementary imaging system which informs ultimate fate of nanoparticle upon intracellular trafficking. Spatiotemporally directed ferroptosis that utilizes endogenous iron source such ferritins has been reported previously [82], however our study report a use of complementary imaging systems to reveal the intracellular fate of nanoparticles in terms of spatiotemporal tracking, followed by timely triggering by adding exogenous reducing agent for acute ferroptosis. To the best of our knowledge, this is the first report on spatiotemporal tracing of ferroptosis-inducing nanoparticles and its controllability and mechanism. Complementary imaging analysis reveals the intracellular transport of nanoparticles at a single cell level, which ultimately suggest the use of burst supplement of ferrous ions to induce ferroptosis. Although in vivo studies are further required for therapeutic uses as a means of translational medicine, this study provides a new strategy for timely-controlled cell therapy.

Conclusion

Complementary imaging analysis using TEM and CLSM with FCS are established and applied to investigate the cellular uptake process, diffusional states, and intracellular interactions of $Fe_3O_4@SiO_2$ nanoparticles at a single nanoparticle level in live cells. Freely diffusing individual nanoparticles are observed in the cytosol during cellular uptake through both endocytosis and electroporation. However, these cytosolic nanoparticles are more frequently found in electroporatic uptake than passive endocytosis. A larger number of nanoparticles are ultimately localized in the perinuclear region and trapped in large immobile vesicles. Moreover, the number of nanoparticles in each vesicle is quantitatively analyzed, and the vesicle size showed a corresponding increase over time, indicating that both free and vesicle-trapped nanoparticles were physically collected in the perinuclear region for degradative clearance through autophagy. Interestingly, the biochemical inertness of the silica induces cellular autophagy in a non-cytotoxic way. Furthermore, we revealed a triggered ferroptosis mechanism initiated by burst release of ferrous ions in perinuclear regions. Acute ferroptosis is proposed as a means of spatiotemporally controlled cancer cell death by

using biocompatible nanoparticles and reducing agent. Quantitative live cell analysis based on the mobility and intracellular trafficking of the nanoparticles not only provides insights into the mechanisms behind the cell signaling pathways but also suggests design strategies of effective and low cytotoxic nanoparticle-based drug carriers and bioimaging probes.

Materials and methods

Cell culture

A human epithelial carcinoma (HeLa) cell line was obtained from the Korean Cell Line Bank (KCLB). HeLa cells were cultured in a 5% CO_2 humidified atmosphere at 37°C in Dulbecco's modified Eagle's medium (DMEM; Gibco Canada Ltd., Burlington, Canada) supplemented with 10% fetal bovine serum (FBS), 100 U/mL penicillin, and 100 U/mL streptomycin.

Cellular uptake of nanoparticles

Fluorescent $Fe_3O_4@SiO_2$ nanoparticles containing RITC dye were obtained from Biterials Co. Ltd. (Seoul, Korea). To examine the cellular uptake of the nanoparticles through endocytosis, HeLa cells were incubated with the nanoparticles (0.1 mg/mL) for a desired period of time on either a coverglass (Cell Desk LF1, Sumitomo Bakelite, Tokyo, Japan) or a chambered coverglass with eight wells (Nunc, Roskilde, Denmark). To deliver the nanoparticles via electroporation, the Neon™ transfection system (Invitrogen) was used for the cells by adapting the manufacturer's instructions for nanoparticles (0.2 mg/L) instead of DNA. After electroporation, the cells were placed on a Cell Desk LF1 in DMEM supplemented with penicillin, streptomycin, and 10% FBS, and maintained at 37ºC under 5% CO_2.

Cell viability assay

Cell viability was determined using EZ-Cytox cell viability assay kits (Daeil Lab Service Co, Seoul, Korea) according to the manufacturer's instructions. Briefly, HeLa cells were suspended at 1×10^4 cells/mL in DMEM medium and 100 μL of the suspension was seeded in the individual wells of a 96-well microculture plate. The cells were allowed to adhere for 24 h. The individual wells were titrated with 10 μL of EZ-Cytox kit reagent in each well then incubated at 37 ºC in a humidified CO_2 incubator for 1 h. After incubation, optical density was measured at a wavelength of 450 nm using an absorbance microplate reader. To evaluate ferroptosis-induced cell viability, cells were treated with desired amount of nanoparticles for 24 h, and further treated with ascorbic acid, DFO, and(or) hydrogen peroxide for 6 h as indicated (Fig. 8 and Fig. S10). To evaluate the cytotoxic effect of ascorbic acid, cell were treated with ascorbic acid as indicated for 24 h (Fig. S11). The cell viability was then obtained, corresponding to previous protocol. To investigate the lipid peroxidation in the cell, Image-iT Lipid Peroxidation Kit (ThermoFisher) was used following the manufacture's protocol. HeLa cells were treated with or without ascorbic acid for 6 h after nanoparticle treatment for 24 hr, followed by staining with the lipid peroxidation kit. The lipid peroxide (LPO) index was obtained by comparing the fluorescence intensity at 510 nm (presence of LPO) to that at 590 nm (absence of LPO).

Confocal laser scanning microscopy

HeLa cells were cultured in a chambered coverglass with eight wells (Nunc, Roskilde, Denmark) and observed over inverted confocal laser scanning microscopes (LSM510 or LSM880 equipped with the Airyscan super-resolution imaging module; Carl Zeiss, Jena, Germany) to allow laser scanning microscopy (LSM) live cell imaging. Green fluorescent protein (GFP)-tagged LC3 was detected by excitation at 488 nm using a

continuous wave (CW) Ar$^+$ laser through a water-immersion objective lens (C-Apochromat, 40×, 1.2 NA; Carl Zeiss). The fluorescent signal was collected using a 505–530 nm band pass filter for LSM510 or through an oil-immersion lens (63×, 1.40NA Plan-Apochromat Oil DIC M27; Carl Zeiss) using a 495–550 nm filter for LSM880. Fluorescent signals from the nanoparticles containing RITC were detected by excitation at 543 nm using a 585 nm long pass filter for the LSM510 and by excitation at 561 nm using a 570 nm long pass filter for the LSM880. The pinhole diameters for confocal imaging were adjusted to 1 Airy unit for both GFP and RITC. LSM observations were performed at room temperature. To avoid bleed-through effects in double-scanning experiments, GFP and nanoparticles were scanned independently in a multi-tracking mode. Time-lapse fluorescence microscopy videos were taken with the LSM880 equipped with an Airyscan module. Microscopy images and videos obtained from the LSM 880 were processed and analyzed using ZEN2012 software (Carl Zeiss).

Fluorescence correlation spectroscopy and dual color cross-correlation spectroscopy

FCS and fluorescence dual color cross-correlation spectroscopy (FCCS) measurements were all performed with a ConfoCor2 (Carl Zeiss) microscope combined with LSM510. The ConfoCor2 consists of a CW Ar$^+$ and He-Ne laser, a water-immersion objective (C-Apochromat, 40×, 1.2NA; Carl Zeiss), and two channels of avalanche photodiodes (SPCM-200-PQ; EG&G). The nanoparticle and GFP were excited with the 488 and 543 nm laser lines, respectively. The confocal pinhole diameter was adjusted to 70 μm for 488 nm and to 78–90 μm for 543 nm illumination. The emission signals were split by a dichroic mirror (570 nm beam splitter) and detected at 505–530 nm in the green channel for GFP, and at 600–650 nm in the red channel for RITC. Data were analyzed with the ConfoCor2 software as described in a previous study [83]. Briefly, the fluorescence auto-correlation functions of the red and green channels, G_r (τ) and G_g (τ), and the fluorescence cross-correlation function, G_c (τ), were calculated by:

$$G_x(\tau) = 1 + \frac{\langle \delta I_i(t) \cdot \delta I_j(t+\tau) \rangle}{\langle I_i(t) \rangle \langle I_j(t) \rangle}$$

where τ denotes the time delay, I_i the fluorescence intensity of the red channel ($i = r$) or green channel ($i = g$), and G_r (τ), G_g (τ), and G_c (τ) denote the auto-correlation functions of red ($i = j = x = r$), green ($i = j = x = g$), and cross ($i = r, j = g, x = c$) correlation functions, respectively. The acquired G_x (τ) values were fit using a one-, two-, or three-component model:

$$G_x(\tau) = 1 + \frac{1}{N} \sum_i F_i \left(1 + \frac{\tau}{\tau_i}\right)^{-1} \left(1 + \frac{\tau}{s^2\tau_i}\right)^{-1/2}$$

where F_i and τ_i are the fraction and diffusion time of component i, respectively, N is the average number of fluorescent particles in the excitation-detection volume defined by the radius w_0 and the length $2z_0$, and s is the structure parameter representing the ratio $s = z_0/w_0$. The structure parameter was calibrated using the known diffusion coefficient (280 μm^2 s^{-1}) of rhodamine 6 G (Rh6G) standard solution at 25℃ [47, 84]. All measured fluorescence autocorrelation functions (FAFs) were fitted by the software installed on the ConfoCor 2 (Zeiss) system using this model. For fluorescent nanoparticles in solution, FAFs were fitted to a one-component model ($i = 1$). FAFs for Si-FMNPs in living cells were fitted to a one- or two-component model ($i = 2$) with additional triplet terms to estimate the diffusion coefficient. Two-component models were used differently to model the nanoparticles in the cytosol: (i) two diffusion components represent fast diffusion (*i.e.*, free diffusion of single nanoparticles) and slow diffusion (vesicle-trapped diffusion) and (ii) one of the diffusion components is taken to represent a photokinetic term (to represent fluorescence decay). The mean fractional ratio ($F_i =$

2) of diffusing nanoparticles was indicated as a percentage. Immobilized aggregate-induced photobleaching data were excluded from the diffusion analysis. The diffusion coefficients of the nanoparticles in the solutions and cells were determined from the diffusion coefficient of Rh6G (280 μm^2 s^{-1}) and the obtained diffusion times for Rh6G and fluorescence nanoparticles. The diffusion time of component $i_{,i}$ is related to the translational diffusion constant D of component i by:

$$\tau_i = \frac{w_{xy}^2}{4D_i}$$

The diffusion of a spherical molecule is related to various physical parameters by the Stokes-Einstein equation as follows:

$$D_i = \frac{\kappa_B T}{6\pi\eta r_i}$$

where T is the absolute temperature, r_i is the hydrodynamic radius of the spherical molecule, η is the fluid-phase viscosity of the solvent, and k_B is the Boltzmann constant. In analysis of FCCS data, the amplitude of the cross-correlation function was normalized to the amplitude of the autocorrelation function of GFP or RITC to calculate the relative cross-correlation amplitude:

$$\left[G_c(0) - 1 / \left[G_g(0) - 1\right]\right] \text{ or } \left[G_c(0) - 1 / [G_r(0) - 1]\right]$$

Transmission electron microscopy

At a desired time of incubation or electroporation to introduce the nanoparticle uptake into the cells, culture plates were fixed for 30 min with 2.5% glutaraldehyde in 0.1 M sodium cacodylate buffer (pH 7.4). After washing, the cells were post-fixed in 2% O$_s$O$_4$ for 1 h and stained *en bloc* with 2% uranyl acetate in distilled water overnight. They were then dehydrated with a series of ethanol (50%, 60%, 70%, 80%, 90%, 95%, and 100%) for 20 min each and embedded in Spurr's resin [85]. After the resin hardened, the Celldesk was removed from the block. Ultra-thin sections were cut parallel to the bottom of the Celldesk at a nominal thicknesses of 60 nm with an ultramicrotome (MTX-L, RMC) stained with 2% uranyl-acetate in 50% methanol followed by lead citrate, and observed by a Tecnai 12 transmission electron microscope operated at 120 kV (FEI, The Netherlands). For quantitative analyses, the images were aligned by manual montage. The endocytosis-related vesicle area and the number of nanoparticles were determined accordingly. At least five cell profiles were taken from each sample.

Elemental analysis of silicon contents

HeLa cells were treated with nanoparticles (100 μg/mL) and different concentrations of ascorbic acid for a desired time as indicated (Fig. S13). After treatment, cell were harvested, washed, and digested to release silicon ions while non-degraded nanoparticles were separated by centrifugation. Elemental silicon concentrations were measured using inductive coupled plasma optical emission spectroscopy (ICP-OES) and relative amount of silicon ions were determined by comparing the silicon contents found in the cells which was only treated with nanoparticles but ascorbic acid as a standard. The results report the effect of ascorbic acid on the degradation of silica shell.

CRediT authorship contribution statement

Chan-Gi Pack: Conceptualization, Investigation, Writing – original draft, Writing – review & editing, Funding acquisition. **Min Kyo Jung**: Methodology, Investigation, Data curation, Writing – original draft. **Kyunghwan Kim**: Methodology, Investigation, Data curation. **Woo-jung Yoo**: Methodology, Investigation, Validation. **Minjong Kim**: Investigation, Data curation. **Minju Cho**: Methodology, Investigation. **Myoung-Hee Kang**: Data curation, Validation. **Sanghwa Lee**:

Methodology, Data curation. **Jisu Lim**: Methodology, Investigation. **In Ki Kim**: Methodology, Investigation. **Sang-Wook Lee**: Methodology. **Jun Ki Kim**: Supervision, Resources, Investigation, Writing – review & editing, Project administration, Funding acquisition. **Jinmyoung Joo**: Supervision, Resources, Investigation, Writing – original draft, Writing – review & editing, Project administration, Funding acquisition.

Declaration of Competing Interest

The authors declare that they have no known competing financial interests or personal relationships that could have appeared to influence the work reported in this paper.

Data availability

Data will be made available on request.

Appendix A. Supporting information

Supplementary data associated with this article can be found in the online version at doi:10.1016/j.nantod.2024.102242.

References

[1] K. Ulbrich, K. Hola, V. Subr, A. Bakandritsos, J. Tucek, R. Zboril, Targeted drug delivery with polymers and magnetic nanoparticles: covalent and noncovalent approaches, release control, and clinical studies, Chem. Rev. 116 (9) (2016) 5338–5431.

[2] E. Blanco, H. Shen, M. Ferrari, Principles of nanoparticle design for overcoming biological barriers to drug delivery, Nat. Biotechnol. 33 (9) (2015) 941–951.

[3] S. Wilhelm, A.J. Tavares, Q. Dai, S. Ohta, J. Audet, H.F. Dvorak, W.C.W. Chan, Analysis of nanoparticle delivery to tumours, Nat. Rev. Mater. 1 (5) (2016) 16014.

[4] S. Sindhwani, A.M. Syed, J. Ngai, B.R. Kingston, L. Maiorino, J. Rothschild, P. MacMillan, Y.W. Zhang, N.U. Rajesh, T. Hoang, J.L.Y. Wu, S. Wilhelm, A. Zilman, S. Gadde, A. Sulaiman, B. Ouyang, Z. Lin, L.S. Wang, M. Egeblad, W.C. W. Chan, The entry of nanoparticles into solid tumours, Nat. Mater. 19 (5) (2020) 566–575.

[5] Y.H. Cheng, C.L. He, J.E. Riviere, N.A. Monteiro-Riviere, Z.M. Lin, Meta-analysis of nanoparticle delivery to tumors using a physiologically based pharmacokinetic modeling and simulation approach, ACS Nano 14 (3) (2020) 3075–3095.

[6] B.J. Du, M.X. Yu, J. Zheng, Transport and interactions of nanoparticles in the kidneys, Nat. Rev. Mater. 3 (10) (2018) 358–374.

[7] S. Hussain, J. Joo, J. Kang, B. Kim, G.B. Braun, Z.G. She, D. Kim, A.P. Mann, T. Molder, T. Teesalu, S. Carnazza, S. Guglielmino, M.J. Sailor, E. Ruoslahti, Antibiotic-loaded nanoparticles targeted to the site of infection enhance antibacterial efficacy, Nat. Biomed. Eng. 2 (2) (2018) 95–103.

[8] Y. Matsumoto, J.W. Nichols, K. Toh, T. Nomoto, H. Cabral, Y. Miura, R.J. Christie, N. Yamada, T. Ogura, M.R. Kano, Y. Matsumura, N. Nishiyama, T. Yamasoba, Y. H. Bae, K. Kataoka, Vascular bursts enhance permeability of tumour blood vessels and improve nanoparticle delivery, Nat. Nanotechnol. 11 (6) (2016) 533–538.

[9] S.B. Ruan, M.Q. Yuan, L. Zhang, G.L. Hu, J.T. Chen, X.L. Cun, Q.Y. Zhang, Y. T. Yang, Q. He, H.L. Gao, Tumor microenvironment sensitive doxorubicin delivery and release to glioma using angiopep-2 decorated gold nanoparticles, Biomaterials 37 (2015) 425–435.

[10] J.H. Su, H.P. Sun, Q.S. Meng, Q. Yin, P.C. Zhang, Z.W. Zhang, H.J. Yu, Y.P. Li, Bioinspired nanoparticles with NIR-controlled drug release for synergetic chemophotothermal therapy of metastatic breast cancer, Adv. Funct. Mater. 26 (41) (2016) 7495–7506.

[11] X.D. Xu, P.E. Saw, W. Tao, Y.J. Li, X.Y. Ji, S. Bhasin, Y.L. Liu, D. Ayyash, J. Rasmussen, M. Huo, J.J. Shi, O.C. Farokhzad, ROS-responsive polyprodrug nanoparticles for triggered drug delivery and effective cancer therapy, Adv. Mater. 29 (33) (2017) 1700141.

[12] A. Salvati, A.S. Pitek, M.P. Monopoli, K. Prapainop, F.B. Bombelli, D.R. Hristov, P. M. Kelly, C. Aberg, E. Mahon, K.A. Dawson, Transferrin-functionalized nanoparticles lose their targeting capabilities when a biomolecule corona adsorbs on the surface, Nat. Nanotechnol. 8 (2) (2013) 137–143.

[13] Y.S. Jin, D. Kim, H. Roh, S. Kim, S. Hussain, J.Y. Kang, C.G. Pack, J.K. Kim, S. J. Myung, E. Ruoslahti, M.J. Sailor, S.C. Kim, J. Joo, Tracking the fate of porous silicon nanoparticles delivering a peptide payload by intrinsic photoluminescence lifetime, Adv. Mater. 30 (35) (2018) 1802878.

[14] P. Rees, J.W. Wills, M.R. Brown, C.M. Barnes, H.D. Summers, The origin of heterogeneous nanoparticle uptake by cells, Nat. Commun. 10 (2019) 2341.

[15] S. Behzadi, V. Serpooshan, W. Tao, M.A. Hamaly, M.Y. Alkawareek, E.C. Dreaden, D. Brown, A.M. Alkilany, O.C. Farokhzad, M. Mahmoudi, Cellular uptake of nanoparticles: journey inside the cell, Chem. Soc. Rev. 46 (14) (2017) 4218–4244.

[16] M.U. Zahid, L. Ma, S.J. Lim, A.M. Smith, Single quantum dot tracking reveals the impact of nanoparticle surface on intracellular state, Nat. Commun. 9 (2018) 1830.

[17] B. Pelaz, P. del Pino, P. Maffre, R. Hartmann, M. Gallego, S. Rivera-Fernandez, J. M. de la Fuente, G.U. Nienhaus, W.J. Parak, Surface functionalization of nanoparticles with polyethylene glycol: effects on protein adsorption and cellular uptake, ACS Nano 9 (7) (2015) 6996–7008.

[18] S. Ohta, D. Glancy, W.C.W. Chan, DNA-controlled dynamic colloidal nanoparticle systems for mediating cellular interaction, Science 351 (6275) (2016) 841–845.

[19] V. Mirshafiee, R. Kim, S. Park, M. Mahmoudi, M.L. Kraft, Impact of protein pre-coating on the protein corona composition and nanoparticle cellular uptake, Biomaterials 75 (2016) 295–304.

[20] W.G. Kreyling, A.M. Abdelmonem, Z. Ali, F. Alves, M. Geiser, N. Haberl, R. Hartmann, S. Hirn, D.J. de Aberasturi, K. Kantner, G. Khadem-Saba, J. M. Montenegro, J. Rejman, T. Rojo, I.R. de Larramendi, R. Ufartes, A. Wenk, W. J. Parak, In vivo integrity of polymer-coated gold nanoparticles, Nat. Nanotechnol. 10 (7) (2015) 619–623.

[21] Y. Wang, Y.X. Lin, Z.Y. Qiao, H.W. An, S.L. Qiao, L. Wang, R.P.Y.J. Rajapaksha, H. Wang, Self-assembled autophagy-inducing polymeric nanoparticles for breast cancer interference in-vivo, Adv. Mater. 27 (16) (2015) 2627–2634.

[22] J. Zhang, Z. Zou, B. Wang, G. Xu, Q. Wu, Y.C. Zhang, Z.Y. Yuan, X. Yang, C. Yu, Lysosomal deposition of copper oxide nanoparticles triggers HUVEC cells death, Biomaterials 161 (2018) 228–239.

[23] N. Oh, J.H. Park, Endocytosis and exocytosis of nanoparticles in mammalian cells, Int J. Nanomed. 9 (2014) 51–63.

[24] S.L. Zhang, H.J. Gao, G. Bao, Physical principles of nanoparticle cellular endocytosis, ACS Nano 9 (9) (2015) 8655–8671.

[25] L. Yu, C.K. McPhee, L.X. Zheng, G.A. Mardones, Y.G. Rong, J.Y. Peng, N. Mi, Y. Zhao, Z.H. Liu, F.Y. Wan, D.W. Hailey, V. Oorschot, J. Klumperman, E. H. Baehrecke, M.J. Lenardo, Termination of autophagy and reformation of lysosomes regulated by mTOR, Nature 465 (7300) (2010) 942–946.

[26] J.J. Li, D. Hartono, C.N. Ong, B.H. Bay, L.Y.L. Yung, Autophagy and oxidative stress associated with gold nanoparticles, Biomaterials 31 (23) (2010) 5996–6003.

[27] Q. Zhang, W.J. Yang, N. Man, F. Zheng, Y.Y. Shen, K.J. Sun, Y. Li, L.P. Wen, Autophagy-mediated chemosensitization in cancer cells by fullerene C60 nanocrystal, Autophagy 5 (8) (2009) 1107–1117.

[28] O. Seleverstov, O. Zabirnyk, M. Zscharnack, L. Bulavina, M. Nowicki, J. M. Heinrich, M. Yezhelyev, F. Emmrich, R. O'Regan, A. Bader, Quantum dots for human mesenchymal stem cells labeling. A size-dependent autophagy activation, Nano Lett. 6 (12) (2006) 2826–2832.

[29] O. Zabirnyk, M. Yezhelyev, O. Seleverstov, Nanoparticles as a novel class of autophagy activators, Autophagy 3 (3) (2007) 278–281.

[30] Y.X. Xie, J.N. Jiang, Q.Y. Tang, H.B. Zou, X. Zhao, H.M. Liu, D. Ma, C.L. Cai, Y. Zhou, X.J. Chen, J. Pu, P.F. Liu, Iron oxide nanoparticles as autophagy intervention agents suppress hepatoma growth by enhancing tumoricidal autophagy, Adv. Sci. 7 (16) (2020) 1903323.

[31] F. Ge, J. Xue, Y. Du, Y. He, Unmodified single nanoparticles undergo a motion-pattern transition on the plasma membrane before cellular uptake, Nano Today 39 (2021) 101158.

[32] U.C. Anozie, P. Dalhaimer, Molecular links among non-biodegradable nanoparticles, reactive oxygen species, and autophagy, Adv. Drug Deliv. Rev. 122 (2017) 65–73.

[33] L. Ding, Z.B. Zhu, Y.L. Wang, B.Y. Shi, X. Ling, H.J. Chen, W.H. Nan, A. Barrett, Z. L. Guo, W. Tao, J. Wu, X.J. Shi, Intracellular fate of nanoparticles with polydopamine surface engineering and a novel strategy for exocytosis-inhibiting, lysosome impairment-based cancer therapy, Nano Lett. 17 (11) (2017) 6790–6801.

[34] M. Bourdenx, J. Daniel, E. Genin, F.N. Soria, M. Blanchard-Desce, E. Bezard, B. Dehay, Nanoparticles restore lysosomal acidification defects: implications for

Parkinson and other lysosomal-related diseases, Autophagy 12 (3) (2016) 472–483.

[35] N. Mizushima, B. Levine, A.M. Cuervo, D.J. Klionsky, Autophagy fights disease through cellular self-digestion, Nature 451 (7182) (2008) 1069–1075.

[36] Q. Yang, H. She, M. Gearing, E. Colla, M. Lee, J.J. Shacka, Z.X. Mao, Regulation of neuronal survival factor MEF2D by chaperone-mediated autophagy, Science 323 (5910) (2009) 124–127.

[37] Y.J. Zhang, R. Sha, L. Zhang, W.B. Zhang, P.P. Jin, W.G. Xu, J.X. Ding, J. Lin, J. Qian, G.Y. Yao, R. Zhang, F.C. Luo, J. Zeng, J. Cao, L.P. Wen, Harnessing copper-palladium alloy tetrapod nanoparticle-induced pro-survival autophagy for optimized photothermal therapy of drug-resistant cancer, Nat. Commun. 9 (2018) 4236.

[38] S.J. Hawkins, L.A. Crompton, A. Sood, M. Saunders, N.T. Boyle, A. Buckley, A. M. Minogue, S.F. McComish, N. Jimenez-Moreno, O. Cordero-Llana, P. Stathakos, C.E. Gilmore, S. Kelly, J.D. Lane, C.P. Case, M.A. Caldwell, Nanoparticle-induced neuronal toxicity across placental barriers is mediated by autophagy and dependent on astrocytes, Nat. Nanotechnol. 13 (5) (2018) 427–433.

[39] H.H. Gustafson, D. Holt-Casper, D.W. Grainger, H. Ghandehari, Nanoparticle uptake: the phagocyte problem, Nano Today 10 (4) (2015) 487–510.

[40] D. Tarn, C.E. Ashley, M. Xue, E.C. Carnes, J.I. Zink, C.J. Brinker, Mesoporous silica nanoparticle nanocarriers: biofunctionality and biocompatibility, Acc. Chem. Res 46 (3) (2013) 792–801.

[41] C. Argyo, V. Weiss, C. Brauchle, T. Bein, Multifunctional mesoporous silica nanoparticles as a universal platform for drug delivery, Chem. Mater. 26 (1) (2014) 435–451.

[42] J.G. Croissant, Y. Fatieiev, N.M. Khashab, Degradability and clearance of silicon, organosilica, silsesquioxane, silica mixed oxide, and mesoporous silica nanoparticles, Adv. Mater. 29 (9) (2017) 1604634.

[43] F. Zhao, Y. Zhao, Y. Liu, X.L. Chang, C.Y. Chen, Y.L. Zhao, Cellular uptake, intracellular trafficking, and cytotoxicity of nanomaterials, Small 7 (10) (2011) 1322–1337.

[44] K. Kim, W.G. Lee, Electroporation for nanomedicine: a review, J. Mater. Chem. B 5 (15) (2017) 2726–2738.

[45] P. Tiefenboeck, J.A. Kim, J.C. Leroux, Intracellular delivery of colloids: past and future contributions from microinjection, Adv. Drug Deliv. Rev. 132 (2018) 3–15.

[46] F. Lu, S.H. Wu, Y. Hung, C.Y. Mou, Size effect on cell uptake in well-suspended, uniform mesoporous silica nanoparticles, Small 5 (12) (2009) 1408–1413.

[47] C.G. Pack, M.R. Song, E. Lee Tae, M. Hiroshima, K.H. Byun, J.S. Kim, Y. Sako, Microenvironments and different nanoparticle dynamics in living cells revealed by a standard nanoparticle, J. Control Release 163 (3) (2012) 315–321.

[48] T. Kalwarczyk, N. Ziebacz, A. Bielejewska, E. Zaboklicka, K. Koynov, J. Szymanski, A. Wilk, A. Patkowski, J. Gapinski, H.J. Butt, R. Holyst, Comparative analysis of viscosity of complex liquids and cytoplasm of mammalian cells at the nanoscale, Nano Lett. 11 (5) (2011) 2157–2163.

[49] W. Jiang, B.Y. Kim, J.T. Rutka, W.C. Chan, Nanoparticle-mediated cellular response is size-dependent, Nat. Nanotechnol. 3 (3) (2008) 145–150.

[50] B.D. Chithrani, A.A. Ghazani, W.C. Chan, Determining the size and shape dependence of gold nanoparticle uptake into mammalian cells, Nano Lett. 6 (4) (2006) 662–668.

[51] Y. Shan, S. Ma, L. Nie, X. Shang, X. Hao, Z. Tang, H. Wang, Size-dependent endocytosis of single gold nanoparticles, Chem. Commun. 47 (28) (2011) 8091–8093.

[52] A.A. de Thomaz, D.B. Almeida, V.B. Pelegati, H.F. Carvalho, C.L. Cesar, Measurement of the hydrodynamic radius of quantum dots by fluorescence correlation spectroscopy excluding blinking, J. Phys. Chem. B 119 (11) (2015) 4294–4299.

[53] J.C. Charpentier, D. Chen, P.E. Lapinski, J. Turner, I. Grigorova, J.A. Swanson, P. D. King, Macropinocytosis drives T cell growth by sustaining the activation of mTORC1, Nat. Commun. 11 (1) (2020) 180.

[54] H. Meng, S. Yang, Z.X. Li, T. Xia, J. Chen, Z.X. Ji, H.Y. Zhang, X. Wang, S.J. Lin, C. Huang, Z.H. Zhou, J.I. Zink, A.E. Nel, Aspect ratio determines the quantity of mesoporous silica nanoparticle uptake by a small GTPase-dependent macropinocytosis mechanism, ACS Nano 5 (6) (2011) 4434–4447.

[55] J.A. Swanson, Shaping cups into phagosomes and macropinosomes, Nat. Rev. Mol. Cell Biol 9 (8) (2008) 639–649.

[56] P. Verderio, S. Avvakumova, G. Alessio, M. Bellini, M. Colombo, E. Galbiati, S. Mazzucchelli, J.P. Avila, B. Santini, D. Prosperi, Delivering colloidal nanoparticles to mammalian cells: a nano-bio interface perspective, Adv. Health Mater. 3 (7) (2014) 957–976.

[57] N. Mizushima, T. Yoshimori, B. Levine, Methods in mammalian autophagy research, Cell 140 (3) (2010) 313–326.

[58] X. Ma, Y. Wu, S. Jin, Y. Tian, X. Zhang, Y. Zhao, L. Yu, X.J. Liang, Gold nanoparticles induce autophagosome accumulation through size-dependent nanoparticle uptake and lysosome impairment, ACS Nano 5 (11) (2011) 8629–8639.

[59] X.D. Zhang, Y.C. Dong, X.W. Zeng, X. Liang, X.M. Li, W. Tao, H.B. Chen, Y.Y. Jiang, L. Mei, S.S. Feng, The effect of autophagy inhibitors on drug delivery using biodegradable polymer nanoparticles in cancer treatment, Biomaterials 35 (6) (2014) 1932–1943.

[60] X.D. Zhang, Y. Yang, X. Liang, X.W. Zeng, Z.G. Liu, W. Tao, X.J. Xiao, H.B. Chen, L. Q. Huang, L. Mei, Enhancing therapeutic effects of docetaxel-loaded dendritic

copolymer nanoparticles by co-treatment with autophagy inhibitor on breast cancer, Theranostics 4 (11) (2014) 1085–1095.

[61] Y. Takahashi, D. Coppola, N. Matsushita, H.D. Cualing, M. Sun, Y. Sato, C. Liang, J. U. Jung, J.Q. Cheng, J.J. Mule, W.J. Pledger, H.G. Wang, Bif-1 interacts with Beclin 1 through UVRAG and regulates autophagy and tumorigenesis, Nat. Cell Biol. 9 (10) (2007) 1142–1151.

[62] D. Kliosnky, Guidelines for the Use and Interpretation of Assays for Monitoring Autophagy (3rd edition) (vol 12, pg 1, 2015), Autophagy 12(2) (2016) 443-443.

[63] S.K. Mitter, C.J. Song, X.P. Qi, H.Y. Mao, H. Rao, D. Akin, A. Lewin, M. Grant, W. Dunn, J.D. Ding, C.B. Rickman, M. Boulton, Dysregulated autophagy in the RPE is associated with increased susceptibility to oxidative stress and AMD, Autophagy 10 (11) (2014) 1989–2005.

[64] N. Lee, D. Yoo, D. Ling, M.H. Cho, T. Hyeon, J. Cheon, Iron oxide based nanoparticles for multimodal imaging and magnetoresponsive therapy, Chem. Rev. 115 (19) (2015) 10637–10689.

[65] X. Ma, R. Hartmann, D. Jimenez de Aberasturi, F. Yang, S.J.H. Soenen, B. B. Manshian, J. Franz, D. Valdeperez, B. Pelaz, N. Feliu, N. Hampp, C. Riethmuller, H. Vieker, N. Frese, A. Golzhauser, M. Simonich, R.L. Tanguay, X.J. Liang, W. J. Parak, Colloidal gold nanoparticles induce changes in cellular and subcellular morphology, ACS Nano 11 (8) (2017) 7807–7820.

[66] L. Liu, X. Bai, M.-V. Martikainen, A. Kårlund, M. Roponen, W. Xu, G. Hu, E. Tasciotti, V.-P. Lehto, Cell membrane coating integrity affects the internalization mechanism of biomimetic nanoparticles, Nat. Commun. 12 (1) (2021) 5726.

[67] W. Li, G.S. Kaminski Schierle, B. Lei, Y. Liu, C.F. Kaminski, Fluorescent nanoparticles for super-resolution imaging, Chem. Rev. 122 (15) (2022) 12495–12543.

[68] Y. Yan, B. Chen, Q. Yin, Z. Wang, Y. Yang, F. Wan, Y. Wang, M. Tang, H. Xia, M. Chen, J. Liu, S. Wang, Q. Zhang, Y. Wang, Dissecting extracellular and intracellular distribution of nanoparticles and their contribution to therapeutic response by monochromatic ratiometric imaging, Nat. Commun. 13 (1) (2022) 2004.

[69] L. Zhou, C. Dong, L. Ding, W. Feng, L. Yu, X. Cui, Y. Chen, Targeting ferroptosis synergistically sensitizes apoptotic sonodynamic anti-tumor nanotherapy, Nano Today 39 (2021) 101212.

[70] Y. Zhang, J. Zhao, L. Zhang, Y. Zhao, Y. Zhang, L. Cheng, D. Wang, C. Liu, M. Zhang, K. Fan, M. Zhang, A cascade nanoreactor for enhancing sonodynamic therapy on colorectal cancer via synergistic ROS augment and autophagy blockage, Nano Today 49 (2023) 101798.

[71] F. Labat-Moleur, A.M. Steffan, C. Brisson, H. Perron, O. Feugeas, P. Furstenberger, F. Oberling, E. Brambilla, J.P. Behr, An electron microscopy study into the mechanism of gene transfer with lipopolyamines, Gene Ther. 3 (11) (1996) 1010–1017.

[72] A.F. Adler, K.W. Leong, Emerging links between surface nanotechnology and endocytosis: impact on nonviral gene delivery, Nano Today 5 (6) (2010) 553–569.

[73] A. El-Sayed, H. Harashima, Endocytosis of gene delivery vectors: from clathrin-dependent to lipid raft-mediated endocytosis, Mol. Ther. 21 (6) (2013) 1118–1130.

[74] M.J. Byun, J. Lim, S.-N. Kim, D.-H. Park, T.-H. Kim, W. Park, C.G. Park, Advances in nanoparticles for effective delivery of RNA therapeutics, BioChip J. 16 (2) (2022) 128–145.

[75] J.A. Kim, K. Cho, M.S. Shin, W.G. Lee, N. Jung, C. Chung, J.K. Chang, A novel electroporation method using a capillary and wire-type electrode, Biosens. Bioelectron. 23 (9) (2008) 1353–1360.

[76] A. Hamm, N. Krott, I. Breibach, R. Blindt, A.K. Bosserhoff, Efficient transfection method for primary cells, Tissue Eng. 8 (2) (2002) 235–245.

[77] J. Kim, M. Kim, J.Y. Kang, K.W. Bong, N. Choi, The detection of urinary exosomal miRNAs for cancer diagnostics and prognostics, BioChip J. 17 (3) (2023) 308–317.

[78] T. Yu, A. Malugin, H. Ghandehari, Impact of silica nanoparticle design on cellular toxicity and hemolytic activity, ACS Nano 5 (7) (2011) 5717–5728.

[79] B. Halamoda Kenzaoui, C. Chapuis Bernasconi, S. Guney-Ayra, L. Juillerat-Jeanneret, Induction of oxidative stress, lysosome activation and autophagy by nanoparticles in human brain-derived endothelial cells, Biochem. J. 441 (3) (2012) 813–821.

[80] G. Lei, L. Zhuang, B. Gan, Targeting ferroptosis as a vulnerability in cancer, Nat. Rev. Cancer 22 (7) (2022) 381–396.

[81] X. Jiang, B.R. Stockwell, M. Conrad, Ferroptosis: mechanisms, biology and role in disease, Nat. Rev. Mol. Cell Bio 22 (4) (2021) 266–282.

[82] L. Zhu, Y. You, M. Zhu, Y. Song, J. Zhang, J. Hu, X. Xu, X. Xu, Y. Du, J. Ji, Ferritin-hijacking nanoparticles spatiotemporally directing endogenous ferroptosis for synergistic anticancer therapy, Adv. Mater. 34 (51) (2022) e2207174.

[83] C.G. Pack, H. Yukii, A. Toh-e, T. Kudo, H. Tsuchiya, A. Kaiho, E. Sakata, S. Murata, H. Yokosawa, Y. Sako, W. Baumeister, K. Tanaka, Y. Saeki, Quantitative live-cell imaging reveals spatio-temporal dynamics and cytoplasmic assembly of the 26S proteasome, Nat. Commun. 5 (2014) 3396.

[84] Y.J. Reo, Y.W. Jun, S.W. Cho, J. Jeon, H. Roh, S. Singha, M. Dai, S. Sarkar, H. R. Kim, S. Kim, Y. Jin, Y.L. Jung, Y.J. Yang, C. Ban, J. Joo, K.H. Ahn, Systematic study on discrepancy of fluorescent properties between in solutions and in cells: super-bright, environment-insensitive benzocoumarin dyes, Chem. Commun. 56 (2020) 10556–10559.

[85] K.E. Lee, J.H. Kim, M.K. Jung, T. Arii, J.S. Ryu, S.S. Han, Three-dimensional structure of the cytoskeleton in Trichomonas vaginalis revealed new features, J. Electron Microsc. 58 (5) (2009) 305–313.